

Copyright
by
Onur Nihat Demirer
2013

**The Thesis Committee for Onur Nihat Demirer
Certifies that this is the approved version of the following thesis:**

**Two Different Perspectives on Capacitive Deionization Process:
Performance Optimization and Flow Visualization**

**APPROVED BY
SUPERVISING COMMITTEE:**

Supervisor:

Carlos H. Hidrovo

Halil Berberoglu

**Two Different Perspectives on Capacitive Deionization Process:
Performance Optimization and Flow Visualization**

by

Onur Nihat Demirer, B.S.

Thesis

Presented to the Faculty of the Graduate School of

The University of Texas at Austin

in Partial Fulfillment

of the Requirements

for the Degree of

Master of Science in Engineering

The University of Texas at Austin

August 2013

Dedication

To my family, friends and the little girl who happens to be the love of my life.

Acknowledgements

I would like to thank my advisor, Dr. Hidrovo, for all the support and guidance that he has provided throughout this research work. My appreciations are extended to Carlos Rios, Dr. Tae Jin Kim, Dr. Brian Carroll and Collier Miers for always being there whenever I needed academic consultancy or a beer buddy. I would also like to acknowledge the valuable efforts of Rachel Naylor, Rebecca Clifton, Ellen Wilkes, Luis Gutierrez and the rest of Multiscale Thermal Fluids Laboratory group. Finally, I wish to express my gratitude towards Dr. Berberoglu for teaching a very interesting class and graciously serving as my reader.

Abstract

Two Different Perspectives on Capacitive Deionization Process: Performance Optimization and Flow Visualization

Onur Nihat Demirer, M.S.E.

The University of Texas at Austin, 2013

Supervisor: Carlos H. Hidrovo

In this thesis, two different experimental approaches to capacitive deionization (CDI) process are presented. In the first approach, transient system characteristics were analyzed to find three different operating points, first based on minimum outlet concentration, second based on maximum average adsorption rate and third based on maximum adsorption efficiency. These three operating points were compared in long term desalination tests. In addition, the effects of inlet stream salinity and CDI system size have been characterized to assess the feasibility of a commercial CDI system operating at brackish water salinity levels. In the second approach, the physical phenomena occurring inside a capacitive deionization system were studied by laser-induced fluorescence visualization of a “pseudo-porous” CDI microstructure. A model CDI cell was fabricated on a silicon-on-insulator (SOI) substrate and charged fluorophores were used to visualize the simultaneous electro migration of oppositely charged ions and to obtain *in situ* concentration measurements.

Table of Contents

List of Tables	ix
List of Figures	x
Chapter 1: Introduction	1
1.1 Motivation.....	1
1.2 Background on Desalination.....	2
1.3 Background on Capacitive Deionization	3
1.4 Scope of Current Study.....	5
Chapter 2: Transient Performance Optimization of CDI Process.....	8
2.1 Methodology.....	8
2.1.1 Experimental Set-up.....	8
2.1.2 Experimental Procedure.....	11
2.1.3 Characteristic Times	13
2.1.4 Performance Evaluation Criteria.....	17
a. Energy recovery ratio.....	17
b. Amount of salt adsorbed per unit volume of solution treated per unit energy	18
c. Thermodynamic efficiency	18
2.2 Results and Discussion	20
2.2.1 Effect of Timing on System Performance	20
2.2.2 Effect of Solution Concentration on System Performance	24
2.2.3 Effect of CDI System Size on System Performance.....	27
Chapter 3: Laser-Induced Fluorescence Visualization of CDI Process.....	31
3.1 Methodology.....	31
3.1.1 Microfluidic Device Fabrication.....	31
3.1.2 Laser-Induced Fluorescence Microscopy Setup.....	39
3.1.3 Experimental Procedure.....	42
3.1.4 Data Processing.....	47

3.2	Results and Discussion	49
3.2.1	Single Fluorophore LIF: Effects of Electric Field on Bulk Solution Concentration	50
3.2.2	Single Fluorophore LIF: Migration of Ions within Porous Electrodes.....	55
3.2.3	Dual Fluorophore LIF	59
	Chapter 4: Conclusion.....	63
	References.....	66

List of Tables

Table 2.1:	Instrument specifications	11
Table 2.2:	Summary of desalination/regeneration cycle durations.....	14
Table 2.3:	Thermodynamic efficiency results.....	23
Table 2.4:	Summary of performance evaluation at different concentrations.....	24
Table 2.5:	Summary of performance evaluation at different CDI system sizes	27

List of Figures

- Figure 1.1: Overview of CDI operation steps: (a) desalination, (b) regeneration. The colours of porous electrodes represent saturation during desalination and depletion during regeneration.5
- Figure 2.1: Exploded view of the CDI cell assembly. The inlet and outlet fittings, electrode contact screws and mounting bolts are omitted. The two aerogels are separated by a polymer mesh and are supported by titanium electrodes on the backside to decrease contact resistance. Rubber gasket is seated in a separate channel outside the test section.9
- Figure 2.2: Schematic overview of the experimental set-up.11
- Figure 2.3: Transient behavior of various nondimensionalized parameters during a steady test. The outlet concentration over time, ions per energy input, and average adsorption rate during desalination process.14
- Figure 2.4: Concentration and current behavior in a transient test. Oscillations in outlet conductivity have a delay due to the finite volume between CDI cell exit and conductivity probe.16
- Figure 2.5: Energy recovery ratio during regeneration of the capacitive deionization system. Results indicate an inverse proportionality between energy recovery ratio and desalination-regeneration duration. Error bars not shown due to negligible electrical measurement errors.21

Figure 2.6: Number of ions adsorbed during desalination per unit energy input and unit volume per cycle. Comparison between the transient tests operating at three different cycle durations shows t2 to have the highest performance according to this metric. The errors are due to uncertainties in flow rate and conductivity measurements.	22
Figure 2.7: Outlet concentration in steady tests for different CDI system sizes. It is seen that the adsorption capacity increases with system size, but the transient behavior also changes. This is thought to be due to connections (tubing) between CDI cells.	28
Figure 3.1: Schematics of (a) parallel plate CDI cell cross section and (b) top view of the fabricated CDI microstructure (features not to scale). A sample SEM image of the porous electrode is also provided for the case of carbon aerogel.	32
Figure 3.2: Photomasks used in the photolithography step: (a) front side mask of the channel and porous electrodes (seen as totally black due to sub-resolution trench size), (b) back side mask of the electrical contacts and inlet/exit ports.	34
Figure 3.3: Fabrication of main channel and electrode regions by photolithography-etch.	35
Figure 3.4: Backside lithography-etch process.	36
Figure 3.5: Figure 5. Fabrication of contacts and micro-macro interface.	37
Figure 3.6: Overview of final device (features not to scale). (a) Channel and porous electrodes on the front side, (b) electrical contacts and fluid connection on the back side.	39

Figure 3.7: Spectral properties of fluorophores and optics. Vertical green line represents excitation. Blue and red shaded regions indicate collected emission from Fluorescein and SRB respectively	40
Figure 3.8: Overview of the experimental setup	42
Figure 3.9: Calibration curve for emission intensity as a function of solution concentration. Dots indicate measurement points and solid line represents linear least squares regression fit for low optical depth (OD) region	44
Figure 3.10: Sample smoothing fit performed for desalination tests with 4x objective. Measurement points inside the porous structure represent average intensity of 25 pores at that location	48
Figure 3.11a: Asymmetric bulk concentration distribution influenced by electrical field, showing the accumulation of cations at the cathode / bulk solution interface and the depletion of cations from the anode	51
Figure 3.11b: Time dependent concentration profiles within the bulk solution for SRB. The concentration distribution within porous structure is omitted	51
Figure 3.12a: Bulk SRB concentration for desalination tests at different CDI cell potentials. Coion expulsion seen in the first 15 s and rate of concentration decrease is directly related to CDI cell potential	53
Figure 3.12b: Concentration profiles during desalination tests performed at different CDI cell potentials. It is seen that the shift of concentration peak and the asymmetry in concentration profile is directly related to CDI cell potential	53

Figure 3.13: 2D concentration profiles for SRB before (a) and during (b) desalination. Concentration within the electrode rises with ionic adsorption, whereas bulk concentration decreases. The lowest concentration is seen in the depletion region	56
Figure 3.14a: Time dependent concentration distribution within the porous electrode and the bulk solution. Formation of depletion region (t=30-60s), decrease in bulk solution concentration and increase in electrode concentration can be seen. NRMSD values are provided with each concentration profile	57
Figure 3.14b: Total amount of ions stored in the bulk solution and within the porous electrode a function of time during desalination	58
Figure 3.15a: Snapshot of the model CDI cell 150 s after beginning of desalination. SRB (top) and Fluorescein (bottom) concentrations ..	60
Figure 3.15b: Concentration profile across the channel section in Figure 14a. SRB is depleted in anode and concentrated within cathode, with almost uniform bulk concentration. Fluorescein is depleted in the cathode and concentrated within the anode, with most of the Fluorescein concentrated at anode / bulk solution interface.....	60
Figure 3.16: Time lapse of desalination (0s - 150s). (t = 3s) Almost uniform concentration distribution at the beginning of desalination. (t=44s) Coions are expelled from both electrodes and Fluorescein concentration in anode increases significantly. (t=100s) Fluorescein ions migrate further into the electrode to form a depletion region (t=150s) Bulk SRB concentration has not changed noticeably, whereas bulk Fluorescein concentration has shifted towards the anode	62

Chapter 1: Introduction

1.1 MOTIVATION

As the world population continues to increase, recently exceeding 7 billion (Bureau, 2012), it is seen that providing fresh water for this increasing population with the limited natural resources is getting more and more challenging (Anderson, Cudero, & Palma, 2010; Welgemoed & Schutte, 2005). Water is no doubt one of the most fundamental human needs; therefore it is of very high importance. Statistics indicate that around one fifth of world population live in areas of water scarcity, and another one quarter face economic water shortage ("Coping with Water Scarcity: Challenge of the 21st Century," 2007), meaning that effective steps have to be taken, in terms of increasing water supply or managing water demand, to overcome this problem. This research is going to focus on increasing "usable" water supply by desalination, which is a key technology to remove the salts and minerals dissolved in water.

Since 97.5% of the water supplies are saltwater and only 0.3% of freshwater sources are readily drinkable (McGlade, Farrell, & Edens, 2012), desalination is an important technology to increase both the quantity and quality of water supply. It can be used to obtain drinking water from sea water salinity levels, or it can be used to decrease the mineral content of brackish water resources to obtain "softer" drinking water. Significant amount of desalination research has been focused on large scale desalination of high salinity water, but there is also substantial potential in low cost and high efficiency desalination of brackish water to be implemented at a much smaller, local scale to process the large amount of water in estuaries and underground water aquifers (Shiklomanov, 1999).

The issue of water scarcity is the main driving force in desalination research, which also applies to capacitive deionization (CDI), but it should also be noted that CDI is a versatile method and can be applied to solve various problems.

1.2 BACKGROUND ON DESALINATION

Desalination methods are generally grouped according to their basic principles of operation such as thermal, membrane, or electrical processes. Thermal desalination is by far the oldest method and was the first to be commercially viable (Technology & Council, 2008). The general mechanism of this process is the evaporation of a solution, which results in a solid by-product and a vaporized liquid. Once this liquid is condensed, the product will be pure water. However, the high energy of vaporization for water requires that a high level of energy be input into the system (Anderson et al., 2010). Despite this drawback, multistage flash distillation is a common commercial desalination technique (Al-Shammiri & Safar, 1999) and most of the desalinated water around the world is obtained by this technique. In membrane desalination, the liquid can permeate through the membrane in the gas phase, whereas the salt content does not undergo phase change and is therefore blocked. A very simple example to this phenomenon is osmosis through a semi-permeable membrane, where water from the dilute mixture on one side of the membrane permeates to the concentrated side, driven by the osmotic pressure, whereas the total salt content of two sides is constant. If a pressure greater than the osmotic pressure is applied to the concentrated side, water moves in the opposite direction, which is termed as reverse osmosis (RO) (Greenlee, Lawler, Freeman, Marrot, & Moulin, 2009; Malaeb & Ayoub, 2011). This technique is very widely used to separate solutions into a purified stream and a brine stream. Modern technologies have also led to manufacturing of synthetic membranes with the ability to selectively filter certain ions in

a flow (Anderson et al., 2010; Y.-J. Kim & Choi, 2010). Combining cation and anion exchange membranes with an external electric field, a stream can be separated into purified and brine streams, which is called membrane electro-dialysis. Despite the lack of thermal energy input needed in membrane technologies, the driving pressure gradient that must be applied can become significantly large as the pore size of the membrane decreases. Finally, electrical desalination methods rely upon the application of an electric potential to sustain an electric field to facilitate the movement of ions due to electrophoretic forces. The main technique which belongs to this category is CDI, but electro-dialysis can also be included due to the utilization of electricity. However, the main difference between these two methods is that CDI does not rely on membranes and the ions are stored directly within the pores of the electrodes in CDI.

1.3 BACKGROUND ON CAPACITIVE DEIONIZATION

Capacitive deionization is a relatively new technology that was developed in the late 1960s (Johnson & Newman, 1971; Newman, 1968). The general operating principle of the process is quite simple; an electric field causes electrophoresis of charged ions towards their porous counter electrodes and the ions are stored within the pores of the high surface area electrodes as long as the electric field is present. This is completely analogous to the working principle of a supercapacitor, which is why the improvements in electrode technology affect the two applications in a similar manner. The specific surface area, defined as the surface area per mass of the electrode, (or simply the adsorption capacity) of most porous materials have remained limited for a long time (Anderson et al., 2010; Pekala et al., 1998). However, with increasing developments in high surface area materials, most particularly carbide-derived carbons, carbon-based aerogels, carbon veils, graphene and activated carbon electrodes, the capacity to store

ions has reached a level that made CDI a process that could be practical and economically feasible (Lim, Park, Park, & Choi, 2009b; Park et al., 2007; Pekala et al., 1998). State of the art CDI systems have various advantages, the first one being high energy efficiency. Since CDI systems have the capability to store the ions through electrostatic forces, analogous to the storage of electric charge in capacitors, it is possible to recover a portion of input energy while cleaning, or regenerating, the electrodes. Secondly, the system performance shows an increase with decreasing inlet stream concentration (Onur N. Demirer, Naylor, Rios Perez, Wilkes, & Hidrovo, 2013), which means that CDI systems can be cascaded with conventional reverse osmosis (RO) systems to reach high purity levels than that are achieved by RO only. Thirdly, CDI systems can be designed to be low maintenance, because the porous electrodes are not susceptible to irreversible fouling problems seen in ion exchange membranes and contamination can be remedied by alkaline or acidic cleaning solutions (Jayaraj, Desai, Lee, & Sohn, 2004). Finally, the electrical working principles of CDI dictate that it can treat any ionic pollutant, whether it is simply salt or dangerous arsenic, so it is a versatile method.

The operation of a CDI cell is illustrated in Figure 1.1. It can be seen that operation consists of two cycles: (1) desalination, where an external electric potential is applied between electrodes so that the counter ions are electrosorbed onto the porous electrode surface, resulting in decreased outlet concentration. (2) regeneration, where the two electrodes are electrically shorted or connected to an external load (a capacitor, battery or another CDI cell) so that electrical energy is harvested from the cell as the ions are expelled back into the solution, resulting in a higher outlet concentration. These cycles have to be repeated consecutively, because the surface area and ionic capacity of

porous electrodes are limited and electrodes need to be cleaned before they can be reused for ion adsorption.

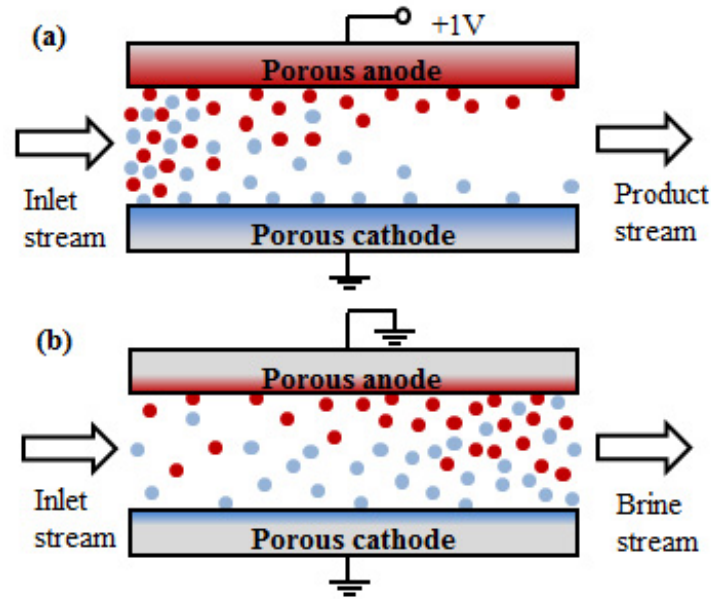


Figure 1.1: Overview of CDI operation steps: (a) desalination, (b) regeneration. The colours of porous electrodes represent saturation during desalination and depletion during regeneration.

1.4 SCOPE OF CURRENT STUDY

When the CDI literature is reviewed, it can be realized that there are some gaps in certain areas, mostly due to the fact that CDI is a relatively new technology, which goes back to 1960s. In this research, two of these areas in CDI literature are identified and studied.

Firstly, performance optimization of CDI process is not a topic which has been investigated thoroughly. This is due to the perception of CDI not being a mature enough technology to be implemented in large scales. Therefore, the research focus has been on understanding and characterizing CDI process and materials (Clifton, Rios Perez, Naylor, & Hidrovo, 2012; Lim, Park, Park, & Choi, 2009a; Prakash, Yeom, Jin, Adesida, &

Shannon, 2006; Ryu, Kim, Lee, & Lee, 2010; L. Wang et al., 2011) and application focused CDI research has remained very low in quantity (Onur N. Demirer et al., 2013). On the other hand, the potential that a CDI system offers can be better realized through proper calibration and operation. For any large-scale operation to be economically feasible, it would need to operate multiple CDI cells consisting of reasonably short, alternating desalination and regeneration cycles (Mossad & Zou, 2012; Villar et al., 2010; Welgemoed & Schutte, 2005). The inefficiencies caused by unoptimized timing of desalination and regeneration cycles would scale up with the system and would be detrimental to economic feasibility of the system. However, the effects of varying the timing of desalination and regeneration processes on the performance of a capacitive deionization system have not yet been examined. In this regard, publications available in the literature focus on varying other operation parameters (such as applied electric potential and solution flow rate) and lack (or not mention) an optimization criteria to select the time when a system will alternate from desalination to regeneration and *vice versa* (Bouhadana, Avraham, et al., 2011; Dermentzis & Ouzounis, 2008; Mossad & Zou, 2012; Villar et al., 2010; Welgemoed & Schutte, 2005; Xu, Drewes, Heil, & Wang, 2008). Therefore, the first part of this research is going to be focused on evaluating the energetic performance optimization of a CDI system at three different brackish salinity levels and three different CDI system sizes to explain the effects of timing, salinity and physical scale on CDI system performance.

Secondly, various physical and empirical electrosorption models have been developed over the years to understand the underlying physics and to estimate the performance of a CDI system. These include various approaches, such as solving the Nernst – Planck equations to estimate ionic adsorption (Biesheuvel, Fu, & Bazant, 2011), using Gouy-Chapman-Stern model to estimate the effect of electrical double layer (EDL)

on electrosorption (Biesheuvel, van Limpt, & van der Wal, 2009), experimentally determining an adsorption velocity for the ions to model the electrosorption (Rios Perez, Demirer, Clifton, Naylor, & Hidrovo, 2013) and using electrical circuit analogies to estimate capacitive behavior of the system during adsorption and desorption processes (Bazant, Thornton, & Ajdari, 2004). However, the basic method to test and verify these results has remained almost the same for four decades and is limited to two types of experimental measurements: (1) Solution concentration is measured at the inlet and outlet of CDI cell to calculate the amount of adsorbed ions, (2) current passing through the external circuit is measured to calculate the energy input during desalination and energy output during regeneration. Therefore, experimental studies still have to treat CDI systems as “black boxes” and the verification of models have to be performed implicitly, based on transient behavior of inlet/outlet concentration and input/output current. Such an approach might be useful to calibrate the models according to various specific CDI systems, but it does not provide any additional insight into the fundamentals of electrosorption process and whether or not the models actually capture the physical phenomena occurring inside the CDI cell correctly. In addition, batch processing CDI systems cannot be monitored by inlet and outlet conductivity probes, since there is no flow of solution during desalination. Finally, the measurements obtained by conventional electrical conductivity probes are only applicable to mixed mean bulk solution concentration and they cannot be used to obtain concentration profiles within the bulk solution and porous electrodes. The main aim of the second part of this research is to demonstrate a novel experimental setup and procedure to understand the CDI process by providing a method to obtain actual ionic transport data from within a model CDI cell.

Chapter 2: Transient Performance Optimization of CDI Process

This study aims to evaluate the energetic performance optimization of a CDI system at three different brackish salinity levels and three different CDI system sizes to explain the effects of timing, salinity and physical scale on CDI system performance. The research presented in this chapter has been published in (Onur N. Demirer et al., 2013) and (Onur N Demirer, Clifton, Perez, Naylor, & Hidrovo, 2013).

2.1 METHODOLOGY

In this section, the experimental CDI setup used for performance testing is presented first. Then, the procedure to conduct and analyze desalination tests is explained. This procedure consists of long term tests, which will be called steady tests, to determine several pivotal points that will later be used to calibrate short and alternating desalination-regeneration processes, which will be called transient tests. The naming “steady” and “transient” is due to the fact that desalination is continued until total electrode saturation so that steady state is reached in the long desalination test, whereas the electrodes are never totally saturated and steady state conditions are never reached in transient tests. Finally, three evaluation criteria are introduced to evaluate the performance of these alternating transient tests.

2.1.1 Experimental Set-up

Experimental investigation about the effects of CDI process on aqueous solutions with low concentrations was conducted in the Multiscale Thermal Fluids Laboratory at The University of Texas at Austin.

Three CDI cells with flat plate electrode configuration were manufactured for energetic analyses at three different CDI system sizes. The outer casing of a CDI cell was constructed from two pieces of acrylic to provide electrical insulation and both pieces

were machined to form a thin inner channel with a rectangular cross-section for fluid flow. Inside the cell, two pieces of high surface area carbon aerogels obtained from Marketch Industries, measuring 25 x 250 mm, were placed on top and bottom faces of the flow channel and both were backed by high conductivity non-corrosive electrodes made of titanium. These carbon aerogels are specified as grade II, containing an approximate surface area of $600 \text{ m}^2\cdot\text{g}^{-1}$ and serve as the ion storage medium for experiments. Between the two pieces of porous carbon aerogels, a polymer mesh was placed to prevent short-circuiting between anode and cathode electrodes, while still allowing proper fluid flow with minimal pressure drop through the cell. The exploded view of CDI cell assembly is presented in Figure 2.1.

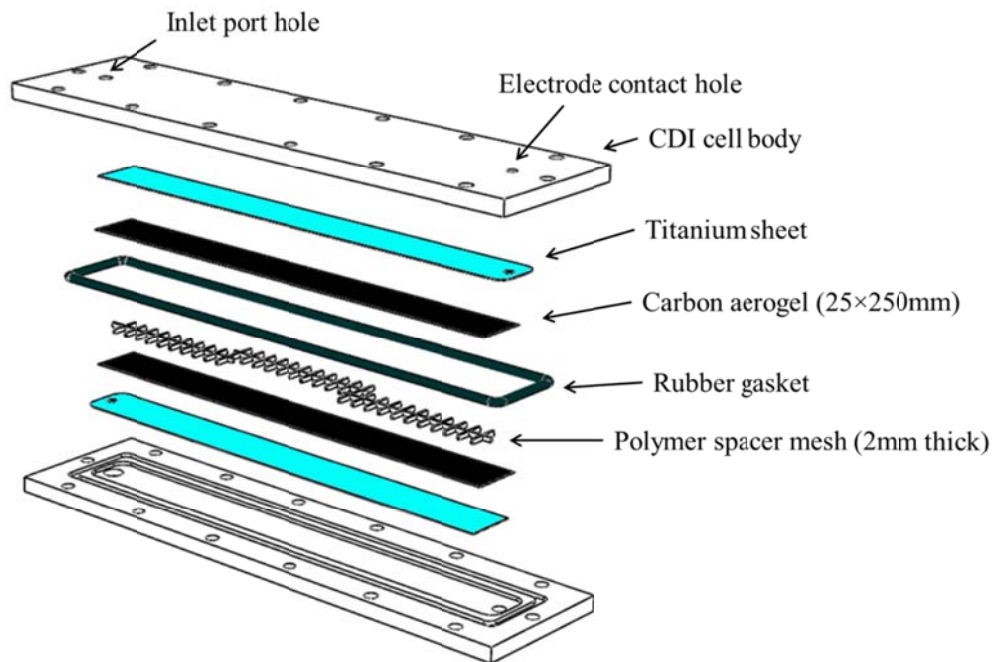


Figure 2.1: Exploded view of the CDI cell assembly. The inlet and outlet fittings, electrode contact screws and mounting bolts are omitted. The two aerogels are separated by a polymer mesh and are supported by titanium electrodes on the backside to decrease contact resistance. Rubber gasket is seated in a separate channel outside the test section.

A schematic overview of experimental setup, similar to (Bouhadana, Ben-Tzion, Soffer, & Aurbach, 2011), is provided in Figure 2.2. The electrical power to the control relay and CDI cell is provided by an Agilent E3647A power supply which is connected to a computer via RS-232 serial port so that it can be controlled and monitored via software. The fluid flow is driven by an Aqua Lifter AW-20 pump and the flow rate is regulated by needle valves downstream of this pump. The flow rate is monitored either directly by an Omega Engineering FLR-1601A flow meter ($\pm 2\%$ accuracy, for low flow rates) or by monitoring the rate of change of mass readings taken by A&D GH-252 analytical balance ($\pm 1.1\%$ accuracy, for high flow rates) placed at the cell outlet. The pressure drop between the inlet and exit of the CDI cell is also monitored by an Omegadyne PX429 pressure transducer. The conductivity of inlet and outlet streams were measured with a pair of eDAQ Flow-Thru Conductivity ET908 sensors ($\pm 0.4\%$ accuracy) connected to the computer via EP357 conductivity isoPods. The desalination or regeneration state for the CDI cell is determined by an NTE Electronics R14 DPDT relay, so that when the relay is powered, anode and cathode of the CDI cell are connected to +1V and ground poles of the power supply respectively, and when the relay is not powered, anode and cathode of the CDI cell were connected through a 30.2Ω resistor. The voltage drop across two ends of this resistor, the flowmeter reading and pressure transducer reading were collected by a National Instruments USB-6008 DAQ and sent to the computer via USB connection. The computer program was developed using National Instruments LabView software and it was used for monitoring and recording inlet and outlet conductivities, desalination and regeneration electric currents, flowmeter readings and pressure transducer readings. In addition, the durations for desalination and regeneration cycles, total number of cycles in a test, relay coil voltage and CDI cell voltage were all set through this program. The specifications for aforementioned instruments are presented in Table 2.1.

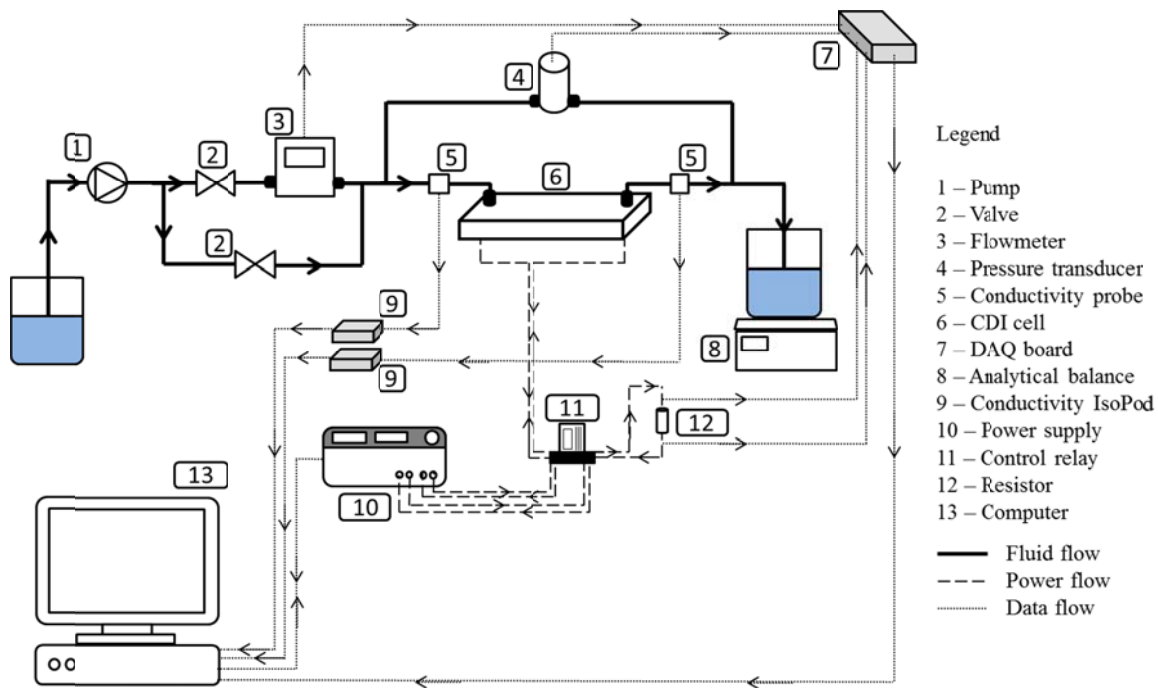


Figure 2.2: Schematic overview of the experimental set-up.

Table 2.1: Instrument specifications

Device		Range	Resolution	Accuracy
Agilent E3647A power supply	Voltage	0 to +35 V	< 5 mV	$\pm 0.05\% + 5 \text{ mV}$
	Current	0 to 0.8 A	< 1 mA	$\pm 0.02\% + 10 \text{ mA}$
Aqua Lifter AW-20 pump	Pressure	0 to $\sim 7.5 \text{ kPa}$	-	-
	Flow rate	0 to $220 \text{ cm}^3/\text{min}$	-	-
Omega Eng. FLR-1601A flowmeter		.01 to 0.5 sccm	.01 sccm	$\pm 2\%$
Omegadyne PX429 pressure transducer		0 to $\sim 2.5 \text{ kPa}$	-	$\pm 0.08\%$
eDAQ ET908 conductivity sensor		0 to 200 mS/m	-	$\pm 0.4\%$

2.1.2 Experimental Procedure

In the present work, two types of desalination experiments were performed: long-term steady tests, and alternating transient tests. A long-term steady desalination was

first performed for every different salinity level and cell size. The data obtained from each steady test was then analyzed to estimate the three time instants later used to switch the system between desalination and regeneration during alternating transient tests. This procedure was first repeated for a single CDI cell system at inlet salinity levels of $0.5 \text{ mg}\cdot\text{cm}^{-3}$, $1.0 \text{ mg}\cdot\text{cm}^{-3}$ and $1.5 \text{ mg}\cdot\text{cm}^{-3}$ to observe the effects of salinity on CDI system performance. Then, tests at $1.0 \text{ mg}\cdot\text{cm}^{-3}$ were repeated for two and three cascaded CDI cells to observe the effects of size scaling on CDI system performance. Then, the results from these transient tests were compared using the metrics introduced later in this section to evaluate the effects of timing, salinity and physical scale on CDI system performance.

The steady desalination tests are performed by applying a constant cell voltage of 1V across the two electrodes of the CDI cell until the porous carbon aerogels are totally saturated. This condition is identified by comparing inlet and outlet conductivities, and thus concentrations. From a control volume perspective, whenever there is a net adsorption of ions within the CDI cell, the outlet concentration should be lower than inlet concentration. This means that the saturation occurs when the outlet concentration rises back up to the inlet concentration level, indicating no net adsorption.

The transient desalination tests are performed by switching the CDI cell between desalination and regeneration at the time instants found by analyzing the steady test data. Approximately fifteen to thirty (depending on cycle duration) transient cycles were included in each transient test, to assure that repeatability among each cycle can be obtained and the initial transients of the cell do not affect the test results. The ionic adsorption, energy input and energy recovery were calculated for every cycle to be used in analysis.

2.1.3 Characteristic Times

By running a steady test, three characteristic times were identified as having the ability to potentially optimize the operation of a transient system. These times correspond to the instants when: the output stream conductivity is minimum, t_1 , the average ionic adsorption rate is maximum, t_2 , and the amount of ions adsorbed per unit energy input into the system is maximum, t_3 . Equations 1 to 3 detail the estimation of these three times.

$$t_1 = t[\min(\sigma)] \quad (2.1)$$

$$t_2 = t \left\{ \max \left[\frac{\int_0^t \frac{N_A}{F \cdot (v^{Cl^-} + v^{Na^+})} (\sigma_0 - \sigma) d\tau}{\int_0^t d\tau} \right] \right\} \quad (2.2)$$

$$t_3 = t \left\{ \max \left[\frac{\int_0^t \frac{N_A \cdot Q}{F \cdot (v^{Cl^-} + v^{Na^+})} (\sigma_0 - \sigma) d\tau}{\int_0^t I \cdot d\tau} \right] \right\} \quad (2.3)$$

Here σ and σ_0 ($S \cdot m^{-1}$) are the outlet and inlet solution conductivities respectively, N_A is Avogadro's number, Q ($m^3 \cdot s^{-1}$) is the solution flow rate, F ($C \cdot mol^{-1}$) is the Faraday's constant, v^{Cl^-} and v^{Na^+} ($m^2 \cdot V^{-1} \cdot s^{-1}$) are chloride and sodium ion mobilities respectively and I (A) is the electrical current that flows through the system during desalination.

The criteria and switching times presented above are illustrated in Figure 2.3. In this figure, the outlet stream conductivity is standardized by its initial value, while the amount of ions adsorbed per unit energy input and the average adsorption rate are standardized by their respective maximum values. The actual times t_1 , t_2 , and t_3 obtained

from these experiments are listed in Table 2.2. These times served to calibrate the switching times for the change from a desalination cycle to the regeneration cycle in a transient experiment.

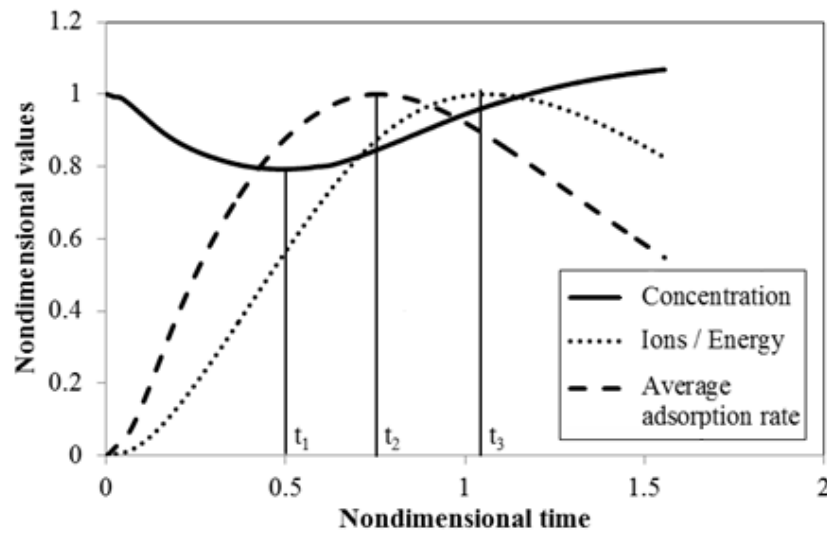


Figure 2.3: Transient behavior of various nondimensionalized parameters during a steady test. The outlet concentration over time, ions per energy input, and average adsorption rate during desalination process.

Table 2.2: Summary of desalination/regeneration cycle durations

	CDI system size		
	1 cell	2 cells	3 cells
Concentration (mg/cm ³)	t ₁ = 1080s t ₂ = 1656s t ₃ = 2204s		
	t ₁ = 860s t ₂ = 1361s t ₃ = 1913s	t ₁ = 934s t ₂ = 2141s t ₃ = 3656s	t ₁ = 5002s t ₂ = 6676s t ₃ = 9679s
	t ₁ = 266s t ₂ = 492s t ₃ = 809s		

Switching the CDI system from desalination to regeneration at the point of minimum outlet concentration, given as t_l in equation 1, is an intuitive choice, as the minimum outlet concentration corresponds to maximum adsorption rate and reaching this point is usually desired. This is the simplest timing point, which will be compared to the optimized timing points given in equations 2 and 3 to quantify possible performance improvements.

The second criterion can be used when the maximum ionic adsorption rate is desired from the CDI system. The adsorption rate of the CDI system is calculated as the product of flow rate and the concentration difference of inlet and outlet solutions, therefore the adsorption rate changes throughout the desalination process. Although maximum instantaneous adsorption rate corresponds to the instant when outlet conductivity is minimized, at time t_l , the maximum average adsorption rate throughout the desalination corresponds to time t_2 , which is expected to be a better measure of overall desalination rate.

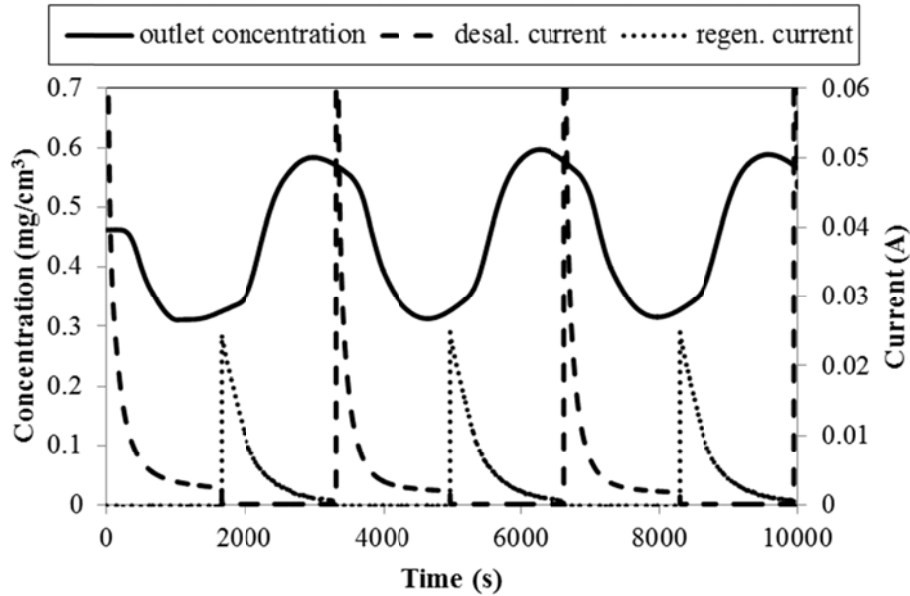


Figure 2.4: Concentration and current behavior in a transient test. Oscillations in outlet conductivity have a delay due to the finite volume between CDI cell exit and conductivity probe.

The final approach is to switch the system from desalination to regeneration at the instant adsorbed ions per input energy is maximized, which corresponds to time t_3 . The main aim of this approach is operating the CDI system at the point of maximum “adsorption efficiency”. This is related to the fact that after some point in desalination, the energy input-ion adsorption behavior of the system follows a diminishing returns behavior, meaning that after time t_3 , continuing the desalination process is not energetically efficient. This effect can be seen when the time behavior of conductivity and input current are observed. The adsorption rate initially increases and then decreases back to zero with electrode saturation, while the input power peaks at the beginning of desalination and decreases to a finite value as the electrodes are saturated. This is due to current leakage between the electrodes through the solution, shown in Figure 2.4.

Before continuing, it must be noted that since the analysis to determine t_1 , t_2 , and t_3 was based on the desalination process, no specific criteria was considered to determine the elapsed time for the regeneration process. Therefore, for this paper, the regeneration and desalination times were set equal to each other for all the cases analyzed. In addition, flow rate was kept constant for every test, therefore the effect of flow rate on system performance is not considered.

2.1.4 Performance Evaluation Criteria

Three criteria were used to evaluate the performance of a CDI system operating in alternating desalination-regeneration transient mode: energy recovery ratio, amount of salt adsorbed per unit volume of solution treated per unit energy, and thermodynamic efficiency.

a. Energy recovery ratio

This criterion relates the magnitude of the desalination energy input to the amount of energy obtained from the CDI cell during its regeneration. The energy delivered to the system during desalination, E_{in} , and recovered during the electrode regeneration, E_{regen} , were estimated as:

$$E_{in} = \int_0^t V \cdot I \cdot d\tau \quad (2.4)$$

$$E_{regen} = \int_0^t I^2 \cdot R \cdot d\tau \quad (2.5)$$

where V is the constant electric potential applied to the desalination cell in volts (1.0 V for this paper), and R is the electric resistance connected to the desalination cell during its regeneration (30.2 ohms). The energy recovery percentage is calculated from the ratio of these values.

One important point to note is that this metric does not take the adsorption performance into account, which indicates that it is a measure of energy consumption, not energy efficiency. Therefore, systems with lower energy recovery ratio might actually have higher energy efficiency, which is the reason for introducing the following two metrics.

b. Amount of salt adsorbed per unit volume of solution treated per unit energy

This standard provides a baseline comparison across the variety of different system configurations and is arguably the best method of extrapolating system performance on a large scale. It is calculated as:

$$\frac{\text{Adsorbed ions}}{\text{Energy} \cdot \text{Volume}} = \frac{N_A \cdot Q}{F \cdot (v^{Cl^-} + v^{Na^+})} (\sigma_0 - \sigma) \cdot \frac{1}{\int_0^t I \cdot d\tau \int_0^t Q \cdot d\tau} \quad (2.6)$$

As seen in the equation above, while producing a large amount of ionic concentration change per unit of solution volume is desirable, it is also important that the energy cost of this change should not be prohibitively large. Both of these effects are considered in this performance metric. However, according to this metric, desalinating a certain amount of ions at different salinity levels result in the same performance, provided the energy consumption and volume of treated solution are equal, which should not be the case. This point is addressed by introducing the thermodynamic efficiency metric, presented below.

c. Thermodynamic efficiency

Thermodynamic efficiency, η_{th} , in the scope of this study is the ratio of reversible work, W_{rev} , needed to separate a saline solution into a dilute product and a concentrated

brine stream, to the net energy requirement, W_{in} , of the experimental capacitive deionization system:

$$\eta_{th} = \frac{W_{rev}}{W_{in}} \quad (2.7)$$

The estimation of the reversible work based on the second law of Thermodynamics is parallel to the energetic analysis presented by Spiegler and El-Sayed for ideal liquid solutions and salt-free product water in five desalination technologies other than capacitive deionization (Spiegler & El-Sayed, 2001). The present paper, however, assesses the desalination process as a separation of the inlet solution into lower salinity product and concentrated brine solutions, which has been demonstrated for multiple effects evaporation (MEE) desalination (Piacentino & Cardona, 2010).

For a constant temperature and pressure desalination process, the reversible work equals the change in Gibbs free energy, ΔG , due to concentration difference. Assuming an ideal solution, the chemical activities in the inlet and outlet streams would equal their molar concentrations. Therefore, the variation in free Gibbs energy can be estimated as (Bejan, 2006):

$$\Delta G = \left(\sum_{out} n_i \cdot RT \ln(x_i) \right) - n_{in} \cdot RT \ln(x_{in}) \quad (2.8)$$

where n (mol) is the amount of solutes passing through the CDI cell, R is the ideal gas constant ($8.31416 \text{ J} \cdot \text{mol} \cdot \text{K}^{-1}$), T (K) is the solution temperature, x is the average molar fraction of the solution (averaged over time in this paper), and the subscripts *in* and *out* denote the inlet stream and outlet streams (either product or brine) respectively.

To validate the ideal solution assumption, the mean ionic activity coefficient, γ_{\pm} , for a $0.5 \text{ mg}\cdot\text{cm}^{-3}$ NaCl solution at 298 K was calculated from the Debye-Huckel theory of electrolytes (Atkins & de Paula, 2006) as 0.96, which is approximately equal to 1 in the scope of this study. Therefore, it can be said that equation 8 is valid for this case. A drawback of using this metric is that it is an indication of desalination efficiency, not desalination rate. Since the desalination rate is addressed by the previous metric, it is expected that these two metrics should be used together to have a better understanding of system performance.

2.2 RESULTS AND DISCUSSION

Performance of a CDI system operating at different desalination and regeneration durations is analyzed for various salinity levels and various CDI system sizes. The results of these analyses are presented in three sections to observe the effects of timing, salinity and scale on CDI system performance independently.

2.2.1 Effect of Timing on System Performance

Three different timing approaches are compared for a single cell CDI system operating at $1.0 \text{ mg}\cdot\text{cm}^{-3}$ inlet salinity level and $0.5 \text{ cm}^3\cdot\text{min}^{-1}$ solution flow rate and the results are presented below.

a) Energy recovery ratio. The energy recovery results, presented in Figure 2.5, reach 40% for a simple experimental CDI cell, which seems promising for the production of an industrial capacitive desalination plant with even greater efficiency. For every test, it is seen that the energy recovery increases during the first cycles and stabilizes at a certain point, after the first 15 cycles for this case.

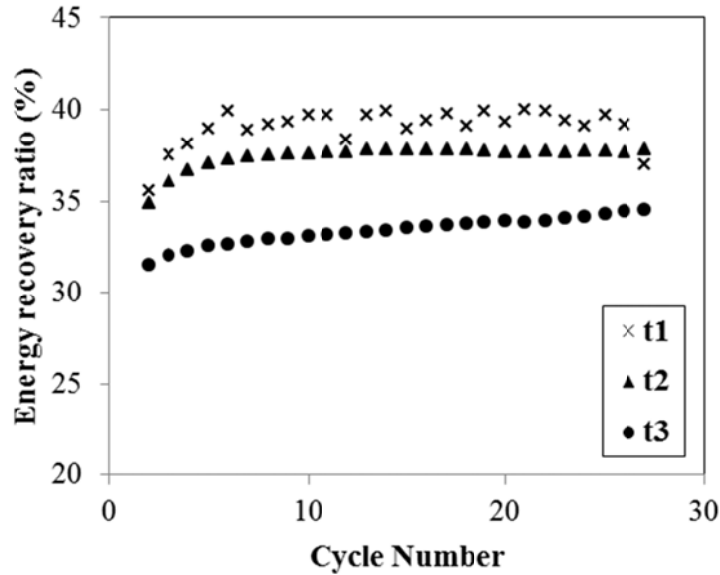


Figure 2.5: Energy recovery ratio during regeneration of the capacitive deionization system. Results indicate an inverse proportionality between energy recovery ratio and desalination-regeneration duration. Error bars not shown due to negligible electrical measurement errors

Calibrating the system at the minimum outlet concentration, t_1 , yields the best energy recovery results, which points to the possibility of t_1 being the most energy efficient timing. Timing the desalination system with respect to maximum energy efficiency, t_3 , results in the worst energy recovery results, whereas timing with respect to maximum average adsorption rate, t_2 , results in an intermediate energy recovery ratio. Comparing these three cases, it is seen that energy recovery ratio is inversely proportional to cycle duration. This is predicted to be due to the leakage current between electrodes during desalination, whose effect becomes more pronounced as the desalination duration increases. This means that desalination-regeneration duration approaching infinity would result in an energy recovery ratio approaching zero.

b) Amount of salt adsorbed per unit volume of solution treated per unit energy.

As seen in Figure 2.6, system calibration with respect to t_2 results in the highest amount

of ions adsorbed per volume per energy for the first 15 cycles. After that, it stabilizes at almost the same performance level as system calibrated with respect to t_3 , albeit still higher. Considering that CDI systems are supposed to operate for many consecutive cycles, it can be said that t_2 results in a slightly higher performance than t_3 according to this metric. System calibration with the timing t_1 results in the worst performance, which is an indication that energy recovery results by themselves are not a good indication of overall system performance, which includes adsorption performance.

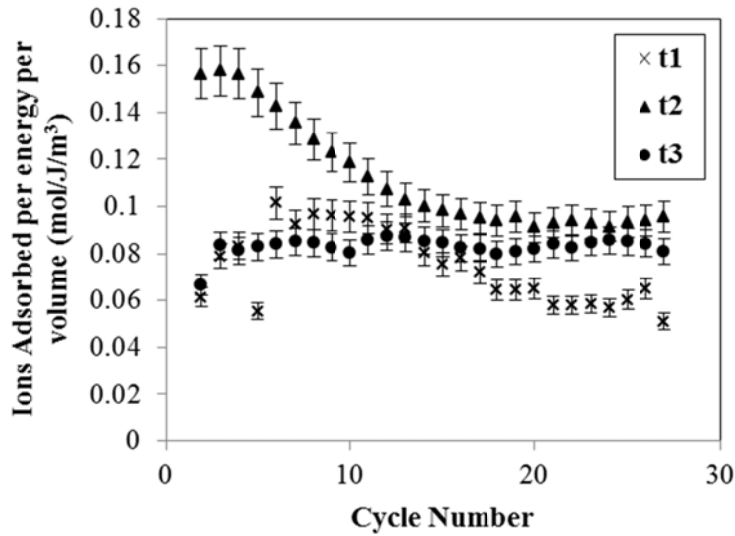


Figure 2.6: Number of ions adsorbed during desalination per unit energy input and unit volume per cycle. Comparison between the transient tests operating at three different cycle durations shows t_2 to have the highest performance according to this metric. The errors are due to uncertainties in flow rate and conductivity measurements.

An interesting point in comparison of the times is seen when adsorbed ions per input energy and adsorbed ions per volume of treated solution are considered separately. It was seen that system calibration with respect to time t_3 results in the highest value of adsorbed ions per input energy, calculated as: $(5.35 \pm 1.11) \cdot 10^{-7}$, $(1.21 \pm 0.25) \cdot 10^{-6}$ and $(1.38 \pm 0.06) \cdot 10^{-6}$ mols \cdot J $^{-1}$ for t_1 , t_2 and t_3 respectively. On the other hand, system

calibration with respect to t_2 results in the highest value of adsorbed ions per volume of solution treated, calculated as: (0.71 ± 0.16) , (1.26 ± 0.30) and (0.97 ± 0.04) $\text{mols} \cdot \text{m}^{-3}$ for t_1 , t_2 and t_3 respectively. This indicates that the operating conditions of the CDI system can be chosen according to specific needs. If the desalination rate is the crucial factor, one should choose to operate the system close to t_2 , with shorter desalination and regeneration cycles. On the other hand, if energy efficiency is the most important factor, one should choose to operate close to t_3 , with longer desalination and regeneration cycles.

c) Thermodynamic efficiency. The thermodynamic efficiency results are presented in Table 2.3 for each desalination/regeneration cycle duration. It is seen that timing t_3 results in the highest thermodynamic efficiency, with t_2 showing somewhat inferior performance. Timing with respect to minimum outlet conductivity, however, results in a thermodynamic efficiency value 0.19%, which significantly less than the other two timing methods.

Table 2.3: Thermodynamic efficiency results

Test	Reversible Energy Input (J)	Actual Energy Input (J)	Thermodynamic Efficiency
t_1	0.35	185.2	0.19%
t_2	0.82	232.2	0.35%
t_3	0.91	236.9	0.38%

The results of thermodynamic efficiency calculations are within expectations. Timing t_3 is based on maximizing the energy efficiency of CDI system and therefore results in the highest thermodynamic efficiency. Timing t_2 represents a calibration for maximum adsorption rate; therefore some concession in energy efficiency has to be made, which is seen in the decrease of thermodynamic efficiency from 0.38% to 0.35%.

2.2.2 Effect of Solution Concentration on System Performance

The testing procedure, including timing with respect to three criteria and performance evaluation based on transient tests, was performed for a single CDI cell, constant $0.5 \text{ cm}^3 \cdot \text{min}^{-1}$ solution flow rate and three different inlet solution salinity levels: $0.5 \text{ mg} \cdot \text{cm}^{-3}$, $1.0 \text{ mg} \cdot \text{cm}^{-3}$ and $1.5 \text{ mg} \cdot \text{cm}^{-3}$.

a) *Energy recovery ratio.* The results, tabulated in Table 2.4, indicate that the energy recovery ratio of the system increases with the inlet solution salinity. This can be interpreted as the effect of remnant ions (from previous cycles) inside the porous electrodes on desalination and regeneration, which is more pronounced at higher salinity conditions.

Table 2.4: Summary of performance evaluation at different concentrations

		Energy Recovery (%)	Ions/(Energy·Volume) ($\text{mol}/\text{J}/\text{m}^3$)	Thermodynamic Efficiency (%)	
Concentration (mg/cm^3)	0.5	t ₁	28.5±1.3	0.028±0.003	0.17±0.02
		t ₂	29.1±0.2	0.036±0.003	0.47±0.05
		t ₃	28.2±1.0	0.032±0.004	0.68±0.07
	1.0	t ₁	39.1±1.0	0.075±0.015	0.19±0.02
		t ₂	37.5±0.6	0.092±0.022	0.35±0.04
		t ₃	33.4±0.7	0.086±0.004	0.38±0.04
	1.5	t ₁	63.1±1.0	0.013±0.004	0.03±0.01
		t ₂	52.9±0.6	0.036±0.012	0.07±0.01
		t ₃	46.3±0.5	0.080±0.015	0.1±0.01

If the electrodes are not totally clean at the beginning of desalination, the number of ions adsorbed during the desalination cycle and also the input energy during desalination decreases. However, the total number of ions stored in the electrodes at the end of desalination is still more than it would be for a desalination cycle started with a

completely clean electrode. This causes the regeneration current to increase, therefore increasing the energy recovery ratio. However, as will be discussed later, the decrease in adsorption performance is more than the increase in energy recovery ratio, meaning that an increase in energy recovery ratio by itself does not mean that a system is more efficient.

One might expect to see a decrease in energy recovery ratio as the salinity level increases, because the resistivity of solution would decrease as the salinity increases, causing an increase in the leakage current, mentioned previously. When the desalination current behaviors are compared for individual cycles at different salinity levels, it is seen that the leakage current is indeed greater for higher salinity solutions, but the effect of remnant ions have a greater impact on energy recovery ratio.

b) Amount of salt adsorbed per unit volume of solution treated per unit energy. According to Table 4, it is obvious that there is not a simple trend between this performance metric and solution salinity level.

When the system performance for $0.5 \text{ mg}\cdot\text{cm}^{-3}$ solution and $1.0 \text{ mg}\cdot\text{cm}^{-3}$ solution is observed, it is seen that there is a significant increase in performance as the salinity level is doubled. It is seen that the energy consumption at these conditions were quite close, whereas the number of ions adsorbed were higher and desalination/regeneration cycles were shorter for $1.0 \text{ mg}\cdot\text{cm}^{-3}$ solution. Therefore, it can be said that the performance increases with salinity up to a certain level, due to more effective adsorption at higher salinity levels.

If the same performance comparison is made between $1.0 \text{ mg}\cdot\text{cm}^{-3}$ and $1.5 \text{ mg}\cdot\text{cm}^{-3}$ solutions, the opposite effect is observed. The performance of the system decreases drastically as the salinity is increased from $1.0 \text{ mg}\cdot\text{cm}^{-3}$ to $1.5 \text{ mg}\cdot\text{cm}^{-3}$ and only the timing t_3 results in acceptable performance at $1.5 \text{ mg}\cdot\text{cm}^{-3}$, while still inferior to

1.0 mg·cm⁻³ results. Therefore, it can be deduced that a CDI system of this size is beyond its optimal operation range at such high salinity levels.

The outlet conductivity and desalination/regeneration current data were investigated to find the source of the system inefficiency at high salinity, and it was seen that the decrease in conductivity was significantly lower than the steady test conditions during desalination of 1.5 mg·cm⁻³ solutions. This points to the effect of remnant ions mentioned before, and it is clearly seen at this conductivity level, remnant ions from previous cycles are a significant cause of performance deterioration. This effect is less pronounced when the system is operated at t_3 , the longest time, which is thought to be due to more efficient regeneration of the system.

c) Thermodynamic efficiency. It is clearly seen that the thermodynamic efficiency of the system decreases as inlet solution concentration increases. The first reason for this behavior is that the increase in solution salinity results in a decrease in solution resistivity, and subsequently an increase in leakage current. This increases the energy consumption of the system, resulting in lower thermodynamic efficiency.

One other effect that causes such a decrease in thermodynamic efficiency at higher salinity levels is the outlet conductivity behavior. The outlet conductivity shows a periodic oscillation behavior around the inlet conductivity level, decreasing during desalination and increasing during regeneration, as seen in Figure 2.4. One of the factors that affect the magnitude of these oscillations is the limited electrode surface area and ionic capacity. At low concentrations, the outlet conductivity is significantly decreased during desalination cycles and significantly increased during regeneration, whereas these concentration oscillations get smaller and smaller compared to inlet concentration as it is increased. This has two effects: firstly, the lower magnitude of oscillations decrease the reversible work input necessary and secondly, even if the oscillation magnitudes were the

same, reversible work to cause the same amount of concentration oscillation is lower at higher salinity levels, due to the logarithmic behavior of Gibbs free energy function. These two factors mean that the thermodynamic efficiency of a CDI system decreases with increasing salinity level.

2.2.3 Effect of CDI System Size on System Performance

Three CDI cells of the same specifications have been manufactured and cascaded as needed to measure the performance of CDI system operating at constant $0.5 \text{ cm}^3 \cdot \text{min}^{-1}$ solution flow rate and $1.0 \text{ mg} \cdot \text{cm}^{-3}$ inlet salinity level, for different sizes, using one, two or three cells.

a) *Energy recovery ratio.* As seen in table 2.5, the energy recovery results do not follow a trend with CDI system size. The highest energy recovery values are obtained for the 2 cell system, followed by 1 cell system and 3 cell system in this order. This leads to the conclusion that energy recovery ratio is not directly correlated to CDI system size.

Table 2.5: Summary of performance evaluation at different CDI system sizes

		Energy Recovery (%)	Ions/(Energy·Volume) ($\text{mol}/\text{J}/\text{m}^3$)	Thermodynamic Efficiency (%)	
System size (number of cells)	1	t ₁	39.1±1.0	0.075±0.015	0.19±0.02
		t ₂	37.5±0.6	0.092±0.022	0.35±0.04
		t ₃	33.4±0.7	0.086±0.004	0.38±0.04
	2	t ₁	48.1±2.5	0.025±0.009	0.14±0.01
		t ₂	41.1±0.7	0.049±0.003	0.24±0.03
		t ₃	37.2±1.0	0.059±0.011	0.49±0.05
	3	t ₁	36.6±1.7	0.028±0.007	0.28±0.03
		t ₂	32.2±1.3	0.037±0.004	0.58±0.06
		t ₃	29.4±1.8	0.033±0.006	1.16±0.13

The difference in energy recovery ratios at different CDI system sizes leads to the suspicion that CDI cell assemblies were not up to the same specifications for different tests. However, the CDI cells were disassembled before starting experimentation at each CDI system size, were checked for any corrosion, leakage or fouling and were reassembled using new carbon aerogels of the same size. In addition, contact resistances at the terminals were checked before each test to have a consistent power supply to the system. Therefore, it is thought that the reason to have such a behavior of energy recovery is not experimental inconsistencies, but the change in the system transients at different CDI system sizes, which are seen to be changing with system size in Figure 2.7.

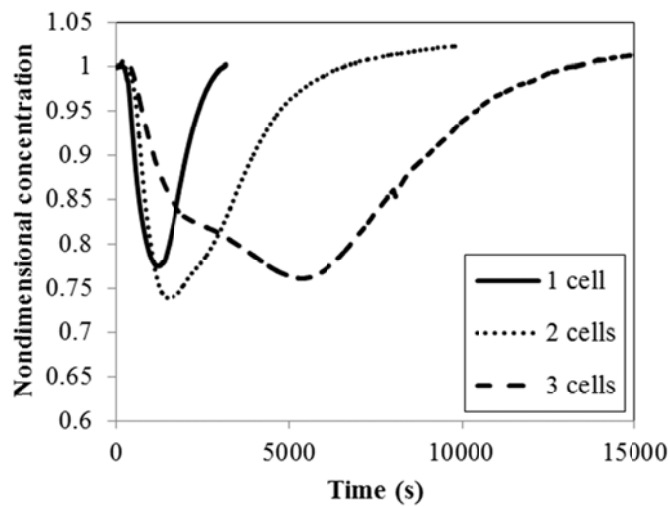


Figure 2.7: Outlet concentration in steady tests for different CDI system sizes. It is seen that the adsorption capacity increases with system size, but the transient behavior also changes. This is thought to be due to connections (tubing) between CDI cells.

One important point to note is that the inverse proportionality between cycle duration and energy recovery is also valid for all three different sized systems. This is in acceptance with the findings in previous sections.

b) Amount of salt adsorbed per unit volume of solution treated per unit energy.

The test results, seen in Table 2.5, indicate that this metric is inversely proportional to the CDI system size. This metric takes both adsorption rate and energy efficiency into account, so the results can be analyzed by considering these effects separately.

When the ionic adsorption performance is compared between 1, 2 and 3 cell systems, it is seen that the amount of ions adsorbed at each cycle is directly proportional to CDI system size, as expected. Using timing t_3 as reference condition, the average amount of ions adsorbed in one cycle is $(1.55 \pm 0.07) \cdot 10^{-5}$, $(3.95 \pm 0.8) \cdot 10^{-5}$ and $(12.0 \pm 2.2) \cdot 10^{-5}$ moles for 1, 2 and 3 cell systems respectively. This increase is associated with the increased cell size and increased cycle durations due to slower saturation of bigger cells. In fact, one can compare the amount of ions adsorbed per volume of solution treated (indicative of adsorption rate) for three cases and see that it is (0.97 ± 0.04) , (1.30 ± 0.27) and (1.50 ± 0.28) $\text{mols} \cdot \text{m}^{-3}$ for 1, 2 and 3 cell systems respectively. This shows that there is an increase in average adsorption rate as the CDI system size increases, due to lower saturation effects.

The average energy consumption per desalination cycle is given as (11.2 ± 0.3) , (21.7 ± 0.7) and (46.3 ± 2.3) J for 1, 2 and 3 cell systems respectively. This indicates an increase in energy consumption with increased system size, which is an expected result of parallel electrical connection of CDI cells.

Combining the two findings above, it is seen that increasing CDI system size results in higher amount of adsorbed ions and higher adsorption rate, but these advantages come at the cost of increased energy consumption. Since the increase in adsorption rate is not as drastic as the energy consumption, increasing CDI system size results in decreased amount of ions per energy input per volume of solution treated. Results of analysis indicate that scaling up is an obvious solution for increasing system

capacity in terms of adsorption rate, but it is not useful for increasing performance with respect to this metric. This emphasizes the importance of system design and optimization at larger scales.

c) *Thermodynamic efficiency*. Results presented in Table 2.5 indicate that thermodynamic efficiency is directly proportional to system size. In addition, it is seen that timing t_3 results in the highest thermodynamic efficiency values for each CDI system size, which is acceptance with the findings presented in section 2.2.1.

The reasoning behind increasing thermodynamic efficiency with CDI system size can be better understood when the transient outlet conductivity behavior of the system is observed. As mentioned in section 2.2.2c, the outlet conductivity shows an oscillating behavior around inlet conductivity, decreasing during desalination and increasing during regeneration. The magnitudes of these oscillations were seen to be increasing with increasing CDI system size. This is an expected result, due to higher ionic capacity of the larger system and longer cycle durations. The increase in magnitude of oscillation of outlet conductivity means that not only the amount of adsorbed ions are increasing, but also the reversible energy required per adsorbed ions is increasing too. This is due to the logarithmic behavior of Gibbs free energy function, as mentioned before. It should be noted that this effect is not included in the calculation of number of ions per input energy per volume of solution treated, therefore the CDI system size dependence of these two metrics are opposite.

The results presented in Table 2.5 seem promising, in the sense that thermodynamic efficiency of the CDI system benefits from upscaling, which is necessary for practical applications.

Chapter 3: Laser-Induced Fluorescence Visualization of CDI Process

In this chapter, an experimental method is introduced to perform simultaneous in situ concentration measurements of both anions and cations during the CDI process and to visualize ion transport within-pseudo-porous electrodes. Using this method, effects of CDI cell potential on bulk solution concentration distribution and electromigration of ions within the porous electrodes are studied. This experimental setup and procedure represents a new visual tool towards understanding the transport phenomena occurring inside a model CDI cell. The research presented in this chapter has been published in (Onur N Demirel & Hidrovo, 2013).

3.1 METHODOLOGY

In this section, details of microfluidic device fabrication, dual fluorophore laser-induced fluorescence (LIF) visualization setup and experimental procedure are provided. Device fabrication is performed in Center for Nano- and Molecular Science and the experiments are conducted in Multiscale Thermal Fluids Laboratory, at The University of Texas at Austin.

3.1.1 Microfluidic Device Fabrication

The top view of the device, presented in Figure 3.1b, is representative of the cross-section of a CDI cell presented in Figure 3.1a. The device consists of a flow channel of 30 mm length, 0.2 mm width and 0.1 mm depth, with pseudo-porous regions on each side of this channel, acting as porous electrodes. These pseudo-porous electrodes include trenches of 10 μm nominal width and 2 mm length, lying perpendicular to the main flow channel. The electrode regions are fabricated to be highly conductive to mimic the high conductivity porous carbon electrodes widely used in CDI applications. Therefore, once an external electric potential is applied onto the contacts, the whole

electrode region becomes charged with minimal resistive loss. In addition, the trenches, or pores, were fabricated not to be straight, but to have roughness elements. This design increases the available adsorption surface area, but also increases the resistance to flow within the pores, which is also the case for porous electrodes used in CDI applications. Therefore, it can be said that the device is a valid representation of a CDI system.

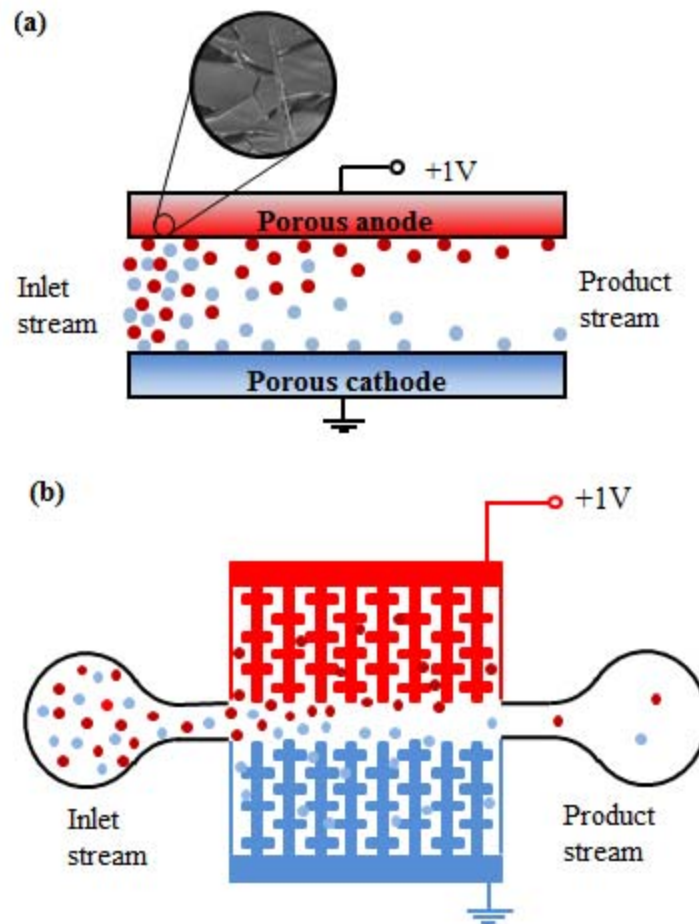


Figure 3.1: Schematics of (a) parallel plate CDI cell cross section and (b) top view of the fabricated CDI microstructure (features not to scale). A sample SEM image of the porous electrode is also provided for the case of carbon aerogel

On the other hand, the electrode structure is called “pseudo-porous”, due to several reasons. Firstly, both the pore size and electrode size are exaggerated, to be able to observe the flow within the porous structure in more detail and to increase the available adsorption surface area, respectively. Due to large pore size, electrical double layers (EDL) within the pores do not overlap, whereas such an occurrence is possible for mesoporous electrodes. Secondly, the electrode structure of the microfluidic device is much more organized than the structure of a conventional porous electrode, which includes pores of irregular shapes and various sizes. Thirdly, the pores are represented as trenches lying perpendicular to the main channel, separated by solid walls. This means that observing electromigration from one pore to another is impossible and only the electromigration effects along the pore orientation is captured. This issue can be solved by using pillar forests instead of trenches, but electrical contacts to pillars can only be obtained from the bottom, which is a challenging task. These restrictions should be considered when interpreting and comparing the results with other CDI applications.

One of the biggest challenges in designing such a microfluidic device is obtaining a strong electric potential difference between the electrodes on each side of the channel, which necessitates having high conductivity porous regions and an insulating channel base. In the case of an actual CDI system, the electrodes are separated by an insulating mesh, seen in Figure 2.1, to prevent contact and current leakage between two electrodes. On the other hand, in a microfluidic system, the two sides have to be connected by the channel base and they cannot be physically disconnected. One solution to this challenge is to have a highly doped surface region with a junction depth close to channel depth. Provided that the substrate is very lightly doped or intrinsic, this should result in low current leakage through channel base. Another solution to this problem is to use a silicon-on-insulator (SOI) wafer as substrate, which has a buried SiO₂ layer between top (device)

and bottom (handle) layers of Silicon. This layer provides insulation between the handle layer and conductive device layer. If the device layer is etched all the way up to this intermediate layer, one might physically divide the device layer into two separate sides, which will serve as the anode and cathode sides. The porous electrodes can then be machined into the anode and cathode sides of the device layer. The intermediate oxide layer also serves as an etch stop during chemical etching of Silicon, so that the channel depth can be specified with an uncertainty of $1\mu\text{m}$. The SOI wafers used in this study have a diameter of 76.2 mm, device thickness of $100\mu\text{m}$ and resistivity of $<.005\Omega\cdot\text{cm}$, handle thickness of $500\mu\text{m}$ and resistivity of $>10,000\Omega\cdot\text{cm}$, with a buried SiO_2 layer of $2\mu\text{m}$ thickness in between these.

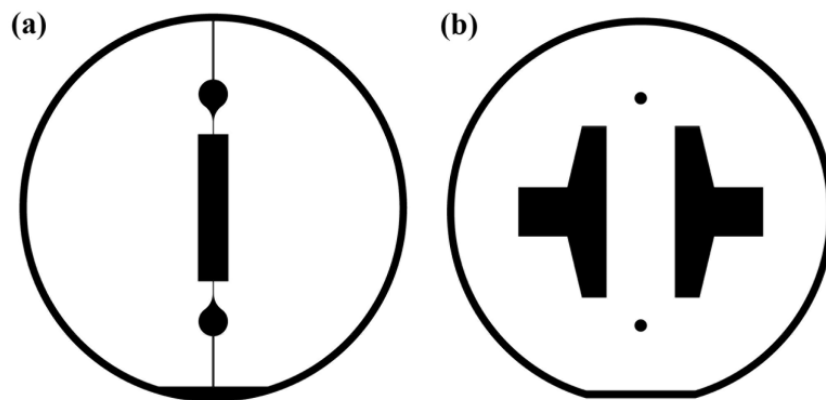


Figure 3.2: Photomasks used in the photolithography step: (a) front side mask of the channel and porous electrodes (seen as totally black due to sub-resolution trench size), (b) back side mask of the electrical contacts and inlet/exit ports

Starting with an SOI wafer, the first step in fabrication process is machining the microchannel and electrodes, and physically separating the device layer into anode and cathode sides. This is performed by contact lithography, using a Suss MA-6 mask aligner, a photomask, shown in Figure 3.2a, printed at 25400 dpi (CAD/Art Services Inc.), SU-8

2025 photoresist and SU-8 Developer (Micro - Chem). The patterned SU-8 is used as a soft mask for Bosch DRIE process performed by Oxford Instruments Plasma Lab 80+ tool. By using alternating C_4F_8 and SF_6 gases in an inductively coupled plasma, the device layer is etched anisotropically down to the buried oxide layer. During this process, C_4F_8 gas is utilized to deposit a passivation layer over the surface to protect sidewalls from etching, while SF_6 gas is used to bombard the wafer surface with ions in the vertical direction (Yang, Zou, Song, & Hao, 2011). Since the SiO_2 etch selectivity in DRIE is around 120-200:1 (Z. Wang et al., 2012), etching is stopped by the intermediate oxide layer and measurements performed by Dektak 6M Stylus profilometer indicate that the channel depth obtained by this process is $100 \pm 1 \mu m$, with near vertical sidewalls and scalloping on the order of $1 \mu m$. This process is illustrated in Figure 3.3.

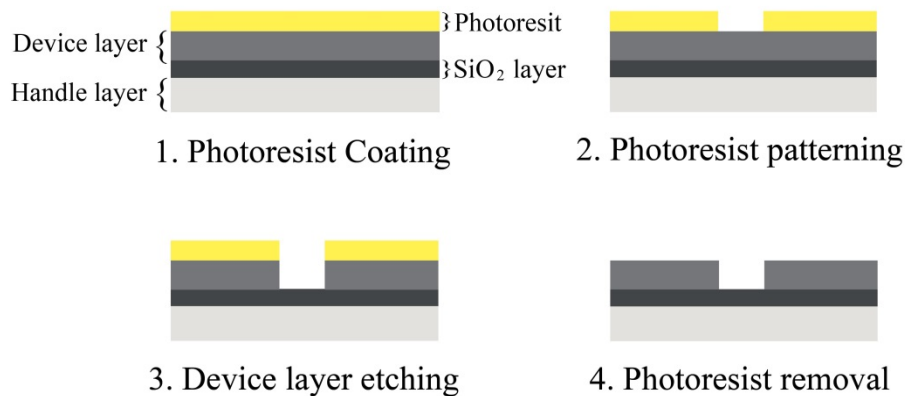


Figure 3.3: Fabrication of main channel and electrode regions by photolithography-etch

Once the micro channel and porous electrodes are machined, a 76.2 mm diameter, 500 μm thick Pyrex wafer was anodically bonded onto the device layer, thus hermetically sealing the channel while providing visual access for visualization from the front side of the microfluidic device. The bonding setup needed for this process consists of a high voltage power supply (ThermoEC EC6000-90), a digital hot plate (Thermo Scientific), a

6”×6”×0.5” aluminum block as anode, a 6”×6”×2” refractory brick for insulation and a stainless steel probe as cathode. Silicon and glass wafers were bonded by following the well-established procedure presented in various publications such as (Albaugh, Cade, & Rasmussen, 1988; Lee, Lee, Liaw, Lao, & Hsing, 2000) and bonding was completed in 2 hours at 800 V and 400°. It should be noted that Si and Pyrex wafer surface qualities are critical for this step; therefore bonding was performed right after the fabrication of micro channel, thus decreasing the chance of surface contamination.

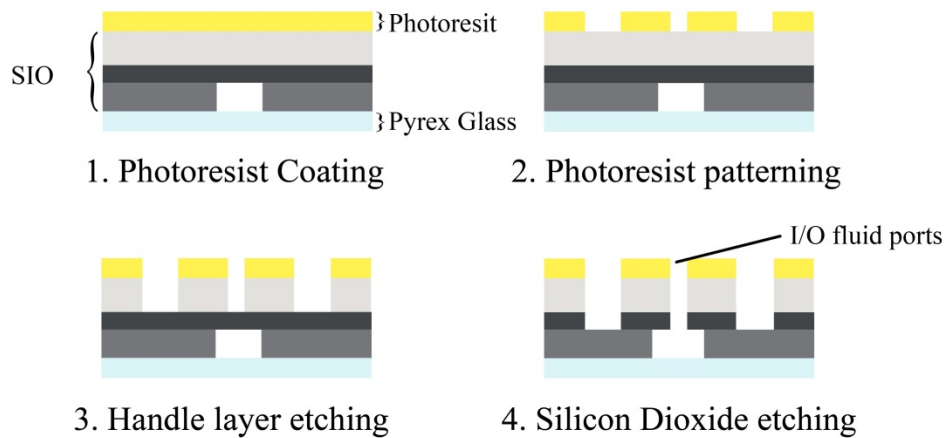


Figure 3.4: Backside lithography-etch process

The next step in fabrication is machining the fluid inlet and outlet ports, in addition to incorporating the electrical contacts, as seen in Figure 3.4. Both the fluid and electrical access to the device are established by a backside etch through the handle layer. The process for backside etch is similar to the first litho-etch step. The soft mask is patterned by contact lithography, using the photomask in Figure 3.2b, and Bosch DRIE is used to etch through the 500 μm thick handle layer. Performing such a backside etch is possible either by a mask aligner with backside alignment feature or a mask containing alignment marks for the wafer itself. The second option was used for the case of this

study and the SOI wafer was aligned with respect to the mask for both the first and second photolithography steps to assure that the front and back side features align correctly. This second etch step is also stopped by the oxide layer, at which point a reactive ion etching (RIE) process was used to etch away the SiO₂ layer to reveal the microchannel inlet/outlet ports and expose the device layer for electrical contacts. The gases used to create the plasma for RIE were CF₄ and O₂.

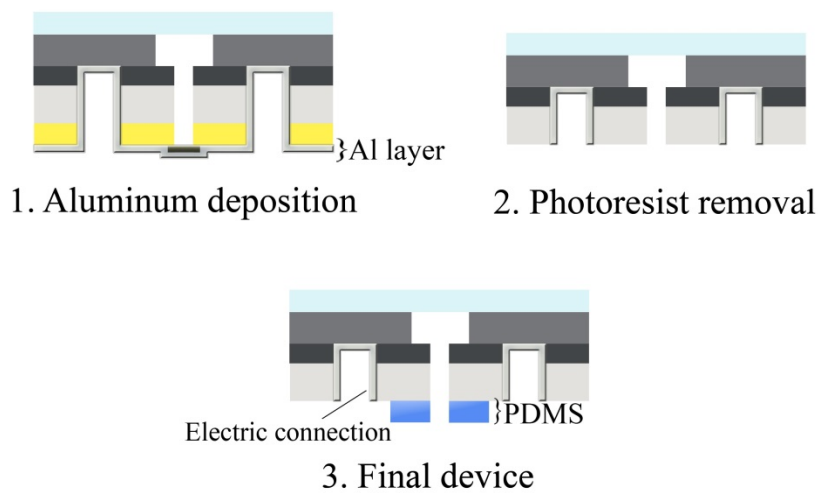


Figure 3.5: Figure 5. Fabrication of contacts and micro-macro interface

After the back etch was completed, SU-8 photoresist was not removed, but instead it was used as a mask in physical vapor deposition (PVD) process, seen in Figure 3.5, to deposit aluminum onto device layer at the electrical contact regions. The inlet and outlet ports were also blocked by temperature resistant Kapton tape to prevent coating and contamination of micro channel. The aluminum pellets (Sigma-Aldrich) were placed inside tungsten boats (Ted Pella, Inc.) and were evaporated by using a Denton Thermal Evaporator, until an aluminum layer of approximately 1 μm was deposited onto the backside of the device. Aluminum deposition is preferred to have a reliable Ohmic

contact onto highly p-doped device layer and it is important that the contact metal is suitable with the type of dopant used in the device layer to prevent having a Schottky contact, which acts as a diode due to the depletion layer at the metal-Si interface.

The final requirement of the microfluidic device is to have a reliable micro-macro fluid interface. At this point, polydimethylsiloxane (PDMS), a popular material in microfluidics, was chosen as interconnect, due to its flexibility, ease of machining and sealing abilities. Firstly, two PDMS slabs were prepared by regular methods present in the literature (Onur N Demirer & Hidrovo, 2013; Milanova, Chambers, Bahga, & Santiago, 2011), and holes at the appropriate diameter to have an interference fit with the tubing were punched in these slabs. Then, these two slabs were bonded on the SOI device by the interlayer bonding method presented in (Quaglio et al., 2008), so that the holes correspond to inlet and outlet ports on the device. The interlayer PDMS at sufficient thickness can seal the surface irregularities on the device and provides a reliable fluid interconnect. Finally, the two ends of the microfluidic channel, which are left open due to the separation of device layer into two, are plugged with PDMS to avoid any fluid leakage.

All the mentioned features (not to scale for easier observation) can be identified in the general overview of the final device shown in Figure 3.6.

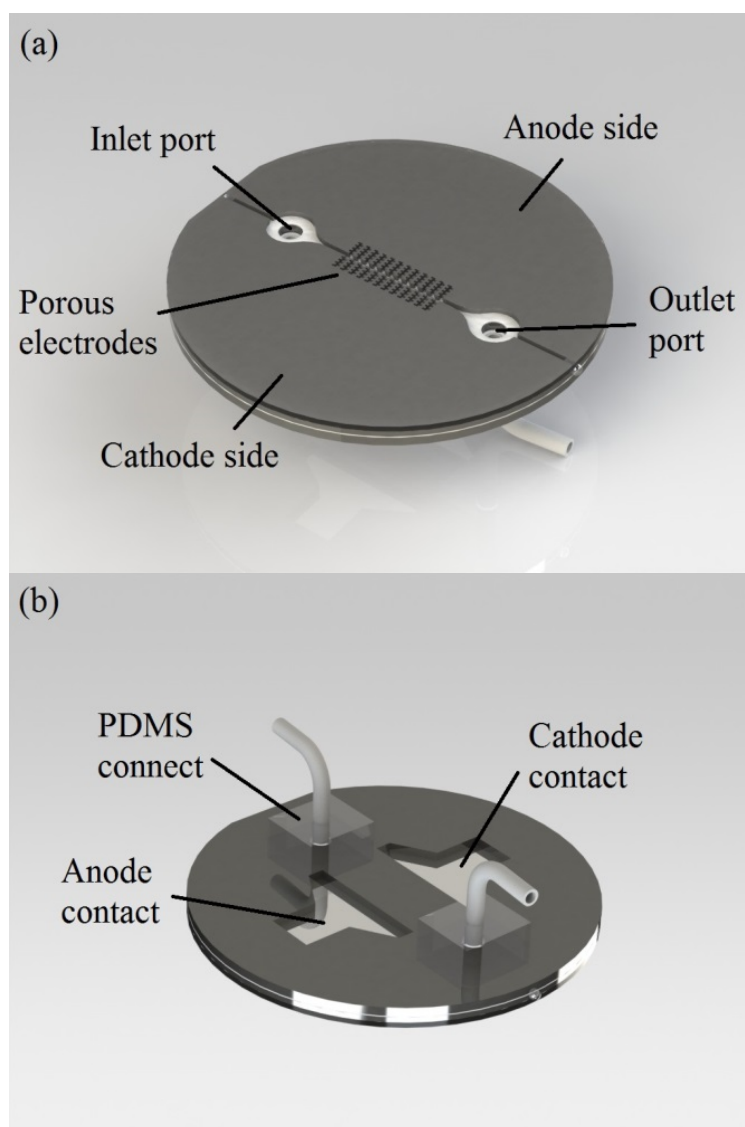


Figure 3.6: Overview of final device (features not to scale). (a) Channel and porous electrodes on the front side, (b) electrical contacts and fluid connection on the back side

3.1.2 Laser-Induced Fluorescence Microscopy Setup

This setup aims to visualize simultaneous transport of cations and anions, therefore a solution containing a cationic dye, Sulforhodamine B (SRB) and an anionic dye, Fluorescein, was used in the experiments. These fluorescent dyes have been

characterized and used in various studies (M. Kim & Yoda, 2010; Ray & Nakahara, 2001; Song, Zhang, Zhang, Shen, & Tang, 2000). They can also be sufficiently excited at 514 nm; therefore only a single illumination source is needed. In addition, their emission and excitation spectra are far enough, so that emission reabsorption problems are minimal and each emission signal can be sufficiently isolated by band pass filters. Spectral information about these dyes and the optics used in their visualization is provided in Figure 3.7.

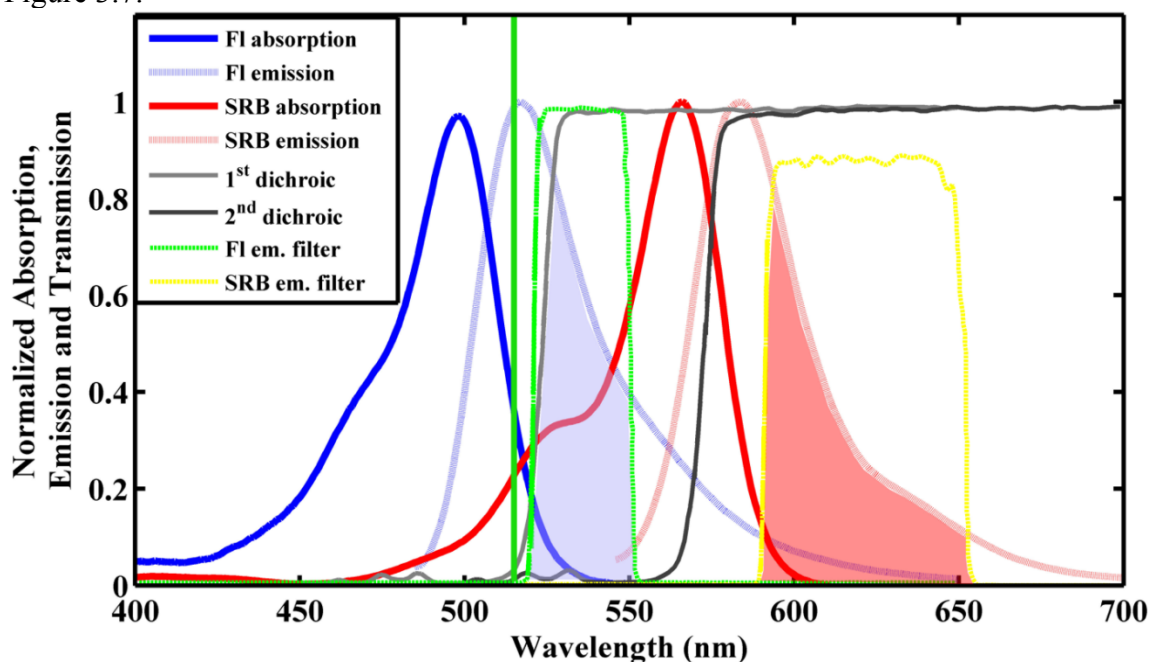


Figure 3.7: Spectral properties of fluorophores and optics. Vertical green line represents excitation. Blue and red shaded regions indicate collected emission from Fluorescein and SRB respectively

An epifluorescence microscope (Nikon Eclipse LV100) was paired with a self-contained multi-line argon ion Laser (Edmund Optics) to have a compact and versatile LIF setup. A dichroic mirror, ZT514rdc (Chroma Technology Corp.), was used to reflect the 514 nm wavelength excitation from the Ar ion laser onto the microfluidic device and

transmit the fluorescence emission from the device above 530 nm wavelength. Since the emission from the device includes both SRB and Fluorescein emissions, they have to be spectrally separated to obtain two separate images of the device. This is performed by a DV2 two channel simultaneous-imaging system (Photometrics), which includes a second dichroic mirror, ZT561rdc (Chroma Technology Corp.), and two emission filters, ET537/29m and HQ620/60m, to separate and isolate the Fluorescein and Sulforhodamine emissions. These two light beams are then reflected onto the imaging array of a Coolsnap HQ CCD camera (Photometrics). Thus, two separate fluorescence images of the same region on the microfluidic device are recorded by a single CCD array by split-field imaging.

To overcome fluid capacitance effects associated with small hydraulic diameters, a pressure driven system was used to provide flow. Beakers containing solutions were placed inside a pressure chamber machined out of Al and chamber pressure was controlled via an electronic pressure regulator (Proportion Air) to modulate flow rate, which was measured by a liquid flow sensor (Sensirion AG). The electric power input for the device was supplied by an E3647A power supply (Agilent).

The overview of this experimental setup is provided in Figure 3.8.

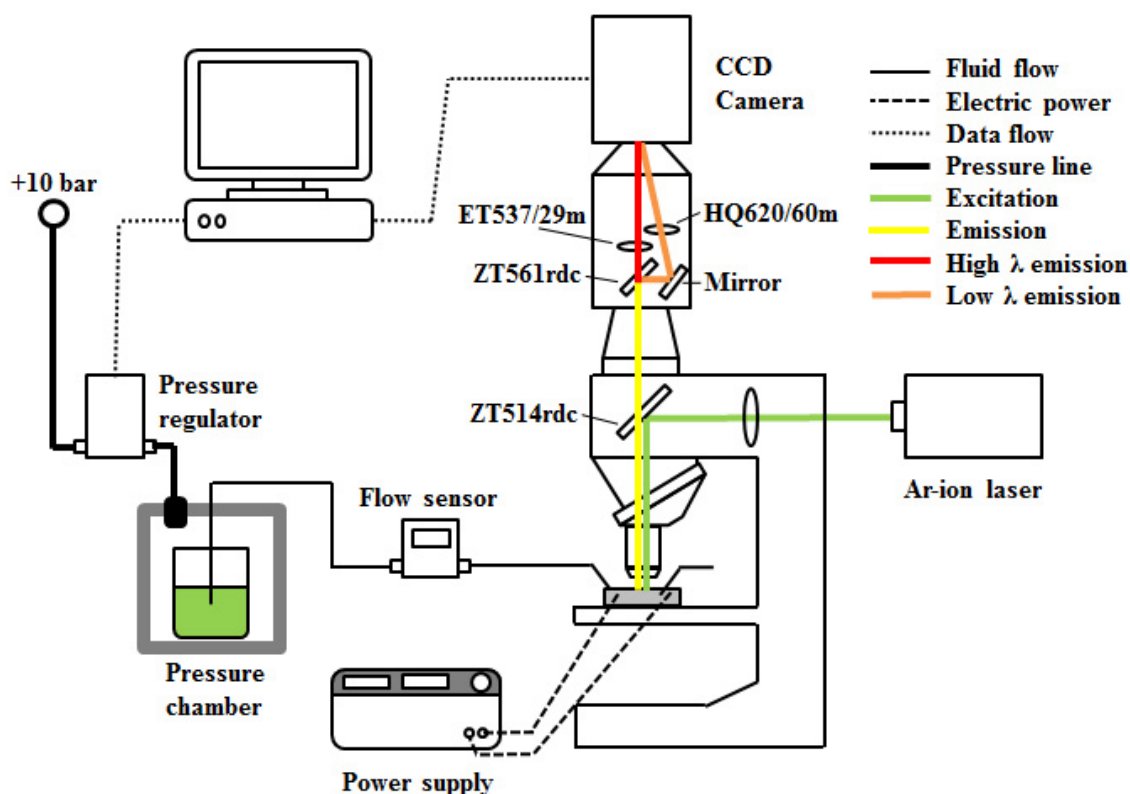


Figure 3.8: Overview of the experimental setup

3.1.3 Experimental Procedure

The microfluidic device, detailed in section 3.1.1, and the LIF microscopy setup, detailed in section 3.1.2, were used in conjunction during the experiments. The microfluidic device was placed on the microscope stage, with front side facing up for visualization. The inlet and outlet fluidic ports on the back side of the device were connected to flow meter outlet tube and a drain tube respectively. Electrical connection was established by applying highly conductive copper tape on the back side electrical contact regions, and soldering the electrical wires onto the copper tape, enabling safe removal and maintenance of electrical contacts without damaging the microfluidic device.

Three types of experiments were performed to prove the functionality of fabricated microfluidic device and LIF visualization setup: (1) high magnification single fluorophore LIF tests, (2) low magnification single fluorophore LIF tests, (3) dual fluorophore LIF tests. In the first type of experiments, SRB was used to examine the effect of electrical potential on the concentration distribution within the bulk solution. A 20x Plan Fluor objective was used to image the main channel with high spatial resolution. Results from these tests were analysed to verify that the new microfluidic device concept is functional and that the electrical field generated by the device is capable of affecting the bulk solution. In the second type of experiments, SRB was used to study the electro migration of ions from bulk solution into the porous structure by using a 4x Plan Fluor objective and imaging both the bulk solution and the porous electrode. The bulk solution concentration decrease due to ionic adsorption onto the porous electrode is also examined. The results from these tests were indicative of the ionic capacity of porous electrodes and overall desalination performance. Third type of experiments were performed by using a mixture of SRB and Fluorescein dyes, to observe the simultaneous behavior of cations and anions during desalination. Both electrodes and the bulk solution were imaged to observe coion expulsion and counter ion adsorption within the electrodes and resulting concentration profiles within the bulk solution.

In all tests, the micro channel was first filled with dye solution and then flow was stopped before applying the electric field, which resembles batch processing with intermittent flow. Therefore, diffusion and electro migration effects were analysed independent of advection. In addition, the model CDI cell was “flushed” with high flow rate solution after each desalination test for several minutes while electrically shorting the electrode regions for regeneration. The CDI cell potential was ranged from 1.5 V to 3.0

V, where the onset of electrolysis is experienced. This points to electrical transmission losses of approximately 50%.

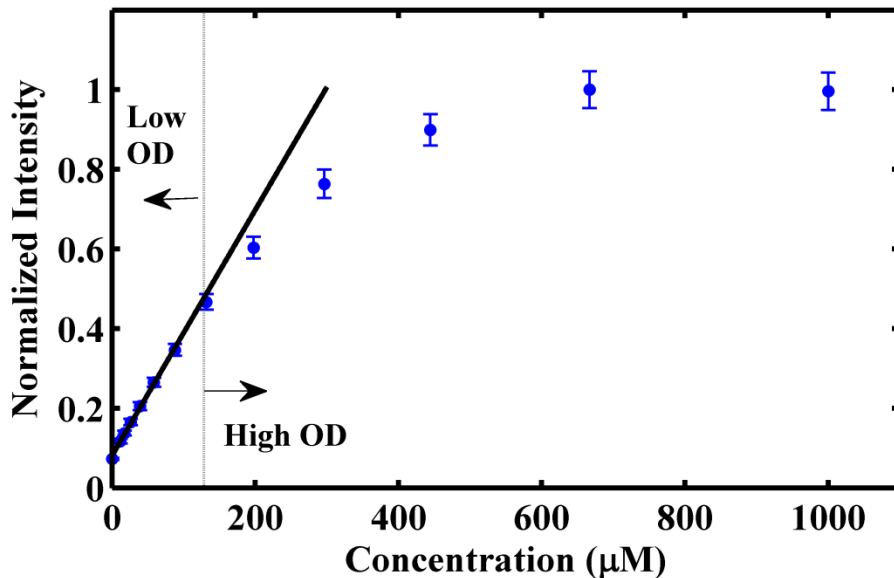


Figure 3.9: Calibration curve for emission intensity as a function of solution concentration. Dots indicate measurement points and solid line represents linear least squares regression fit for low optical depth (OD) region

CDI systems are limited by ionic adsorption capacity of the porous electrodes. Due to this ionic capacity limit, concentration changes due to capacitive deionization are more significant at lower solution concentrations. For this reason, concentrations of Fluorescein and SRB solutions prepared in this study are relatively low. For the first type of tests, 1.5 μM SRB solutions were used, for the second type of tests, 3.0 μM solutions were used to compensate for low NA 4x objective and for the third type of test, 1.5 μM Fluorescein and 0.75 μM SRB solutions were used to have balanced intensity values on both DV-2 channels. Such low fluorophore concentrations mean low optical depth, in which case self-quenching effects are negligible and emission intensity can be linearly related to local concentration (Carroll & Hidrovo, 2012). To verify this assumption, SRB

solutions with various concentrations were prepared and imaged within the microfluidic device. The resultant emission versus concentration behavior is provided in Figure 3.9. As seen in this figure, the linear least squares regression fit lies within the uncertainty bounds of the concentration measurements for concentrations up to 130 μM . Therefore, it can be said that concentration and emission intensity are related linearly. This linearity implies negligible self-quenching effects, so SRB solutions with concentrations up to 130 μM are defined to have low optical depth in the case of this study. Since the low optical depth conditions are met in all of the experiments, “intensity” and “concentration” can be used interchangeably and the calibration equation is given as:

$$I = a \cdot C + b \tag{3.1}$$

where I denotes normalized intensity, C denotes measured concentration and calibration constants a and b are found as $(3.59 \pm 0.08) \cdot 10^{-3}$ and $(94.1 \pm 3.8) \cdot 10^{-3}$ respectively.

For concentrations higher than 130 μM , self-quenching effect starts to become pronounced and the slope of emission versus concentration curve decreases. Therefore, emission versus concentration relationship is not linear anymore and this has to be taken into account during calibration process. If the concentration is increased higher than 700 μM , it is seen that the self-quenching effect becomes even more pronounced and increased concentration reduces emission intensity. Due to this self-quenching effect, the upper bound of the concentrations that can be measured by the method presented in this study is approximately 700 μM , provided that nonlinear emission/concentration behavior is accurately captured.

The main challenge in using low concentration fluorescent dye solutions is the weak emission intensity. Since there is always random noise captured by the imaging system, it is important to have significant emission intensity from the channel to be

visualized, so that signal-to-noise ratio can be kept as high as possible. Considering that the electro migration and diffusion processes are relatively slow, low emission intensities associated with dilute solutions can be remedied by higher exposure time, the duration for which the micropixel array of the CCD camera is exposed to light. This approach increases the captured emission intensity, but, although to a lesser extent, it also increases the noise captured from the environment. In addition, longer exposure times mean lower frame rate and lower temporal resolution, since the system is not capable of sensing the changes occurring in less time than the exposure duration. Therefore, there exists a captured intensity versus noise and temporal resolution trade-off in determination of the optimal exposure time. For the case of this study, exposure time of the images taken with 10x and 20x objectives was chosen as 1s and exposure time of the images taken with 4x objective was chosen as 2s. This adjustment in exposure time is necessary to compensate for the lower numerical aperture (NA) of 4x lens, which results in lower fluorescence emission intensity. The noise problem associated with the increased exposure time for low magnification experiments is solved by using data processing techniques, which are detailed in section 2.4.

All solutions used in this study were prepared by using deionized water as the solvent, because the ions released by buffer solutions contribute to deionization process and interfere with the measurements. Therefore, pH levels cannot be strictly controlled and one should either check the solution pH levels regularly or use fluorophores with good emission stability at a wide pH range to have reliable concentration measurements. Out of these two dyes, Sulforhodamine exhibits pH independent fluorescence emission between 4 and 9, whereas Fluorescein exhibits pH dependent emission. Therefore, single fluorophore tests were performed by SRB and the pH of dual fluorophore mixtures were regularly monitored to overcome emission instability.

3.1.4 Data Processing

Fluorescent radiation emitted by the dyes inside the microfluidic device was recorded into .TIF stacks. These .TIF files were then imported into Matlab to perform image processing. Firstly, background noise, which was measured for an area on the device with no fluorophores, was subtracted from the images. By the removal of background noise, it was assured that all the measured intensity is due to the fluorescent emission. Then, the intensity at every pixel was normalized by the intensity value measured for a uniform concentration dye solution to compensate for the nonuniformity of laser excitation and aberrations in the optical elements. By normalizing the intensities at every pixel, it was assured that the gradients in the measured intensity were not due to the optical system used during the experiments, but due to concentration gradients within the microfluidic device. Such an intensity normalization procedure is not needed if ratiometric techniques are used, so that the ratio of fluorescent intensities of two dyes is considered instead of individual intensities. However, in the case of this study, independent concentration profiles of two different dyes should be known to be able to visualize simultaneous electromigration of oppositely charged particles, so this second data processing step is necessary.

Since the fluorescent dyes have a wide range of emission spectra, it is not practically possible to completely separate the two emissions without using very narrow emission filters, which decrease the emission intensity drastically. This problem is also illustrated in Figure 3.7, where the emission of two dyes overlap within the filtered ranges. To overcome this, the amount of cross-talk between SRB and Fluorescein channels should be characterized, which was performed by imaging two adjacent microfluidic channels, one filled with SRB, one filled with Fluorescein, within the same frame. Average fluorescence intensity that passes on to the other channel was found to be

8.2% for SRB and 10.3% for Fluorescein. Using these two values and the measured intensity profiles, actual concentrations of both dyes were calculated by solving the following 2-by-2 linear system of equations for all the pixels:

$$\begin{bmatrix} 1 & 0.103 \\ 0.082 & 1 \end{bmatrix} \begin{bmatrix} I_{SrB} \\ I_{Fl} \end{bmatrix} = \begin{bmatrix} I_1 \\ I_2 \end{bmatrix} \quad (3.2)$$

where I indicates intensity, subscripts SrB and Fl stand for SRB and Fluorescein and subscripts 1 and 2 indicate the DV-2 channel number. In this configuration, channels 1 and 2 are used to measure the fluorescence intensity of SRB and Fluorescein respectively.

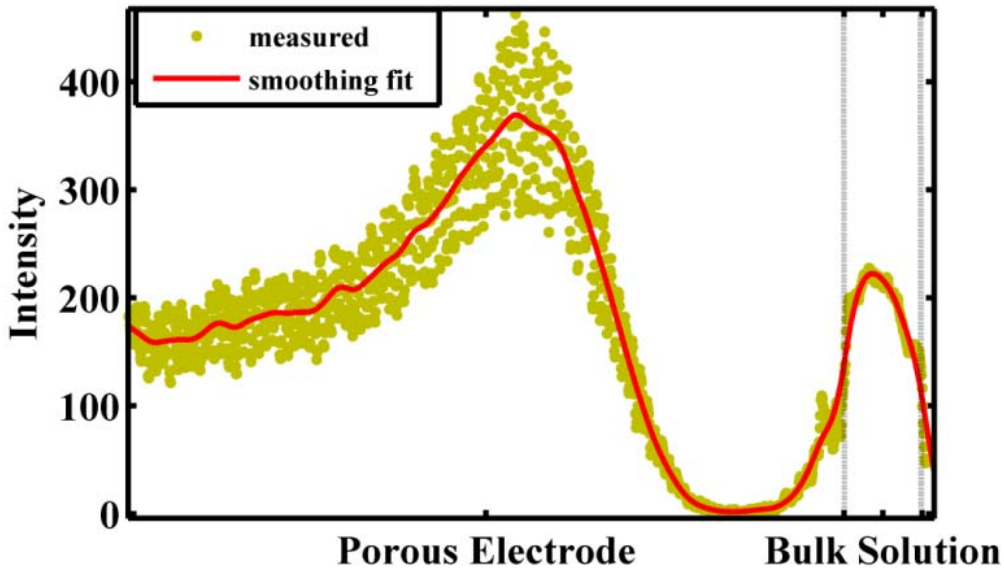


Figure 3.10: Sample smoothing fit performed for desalination tests with 4x objective. Measurement points inside the porous structure represent average intensity of 25 pores at that location

One specific challenge in extracting the concentration from fluorescence intensity measurements is seen in the data processing of desalination tests performed with 4x objective lens. It has been mentioned in the previous section that the captured fluorescence intensity decreases with decreasing NA and higher exposure time was

necessary to overcome this problem. However, increasing the exposure time also increases the background noise. In addition to this noise, the area imaged with the 4x lens is relatively large and spatial resolution within the porous structure is considerably less than high magnification lenses, so it is impossible to draw a straight line through the porous structure and record the concentration along that cross section. Therefore, for low magnification tests, the concentration profiles for 25 separate pores were averaged and a smoothing curve fit was applied to the average concentration profile to overcome noise problems. Such a curve fit process is exemplified in Figure 3.10.

As seen in Figure 3.10, the concentration profile contains random noise. The error due to this noise is characterized by finding the root mean square deviation (RMSD) between the smoothing fit and actual data points and normalizing the RMSD by the range of measured intensities to obtain the normalized RMSD (NRMSD), given by equation 3:

$$NRMSD = \frac{\sqrt{\frac{1}{N} \sum_{i=1}^N (I_i - \hat{I}_i)^2}}{I_{\max} - I_{\min}} \quad (3.3)$$

where N indicates the total number of data points, I indicates measured intensity, \hat{I} indicates smoothing fit intensity, subscripts *max* and *min* indicate the maximum and minimum values in the data set. The NRMSD values obtained by this method are included with the concentration profiles presented in section 3.2.

3.2 RESULTS AND DISCUSSION

The results from all three types of LIF experiments are presented and discussion of the underlying phenomena are provided in this section.

3.2.1 Single Fluorophore LIF: Effects of Electric Field on Bulk Solution Concentration

Single fluorophore LIF experiments were first used to observe the effect of electric field applied by the porous electrode on the bulk solution concentration. This effect has been previously modelled for “symmetric binary electrolytes with equal anion and cation mobilities” (Bazant et al., 2004). However, unlike the findings of this study, which estimate the bulk concentration to decrease symmetrically across the channel, application of the electric field shifted the SRB concentration peak towards the cathode, resulting in an asymmetric concentration profile across the channel, as seen in Figure 3.11a. There are several reasons for such a difference in results. Firstly, the SRB ions are significantly larger than the counter ions they release upon dissolution in water; therefore the symmetric electrolyte assumption does not hold. Secondly, the electrodes in this experimental setup are more complex than the simple case of parallel flat electrodes. Thirdly, and more importantly, the flow of ions into the porous structure is impeded by the presence of the porous structure itself. This physical resistance of porous structure against electro migration can be reduced by having higher porosity electrodes, but it is always present to some degree. This effect has already been taken into account four decades ago (Johnson & Newman, 1971) by defining an “electrode ionic resistance” in an electrical circuit analogy, and more recently (Biesheuvel, Fu, et al., 2011) by defining an “effective diffusion coefficient” of ions within the electrode, which is lower than the diffusion coefficient in the bulk solution. Due to this known effect, the flux of ions from electrode / bulk solution interface towards the porous electrode is less than the flux of ions from bulk solution to electrode / bulk solution interface. Thus, the cations are accumulated at the cathode / bulk solution interface and, for the same reason, they are

depleted from anode / bulk solution interface. This results in the asymmetric concentration profile across the bulk solution, seen in Figure 3.11a.

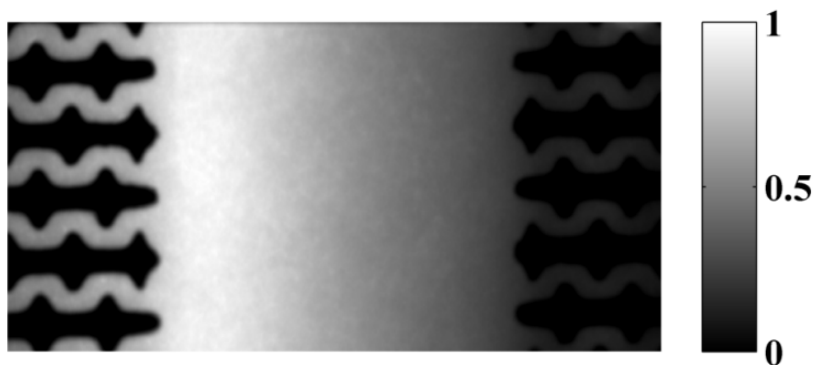


Figure 3.11a: Asymmetric bulk concentration distribution influenced by electrical field, showing the accumulation of cations at the cathode / bulk solution interface and the depletion of cations from the anode

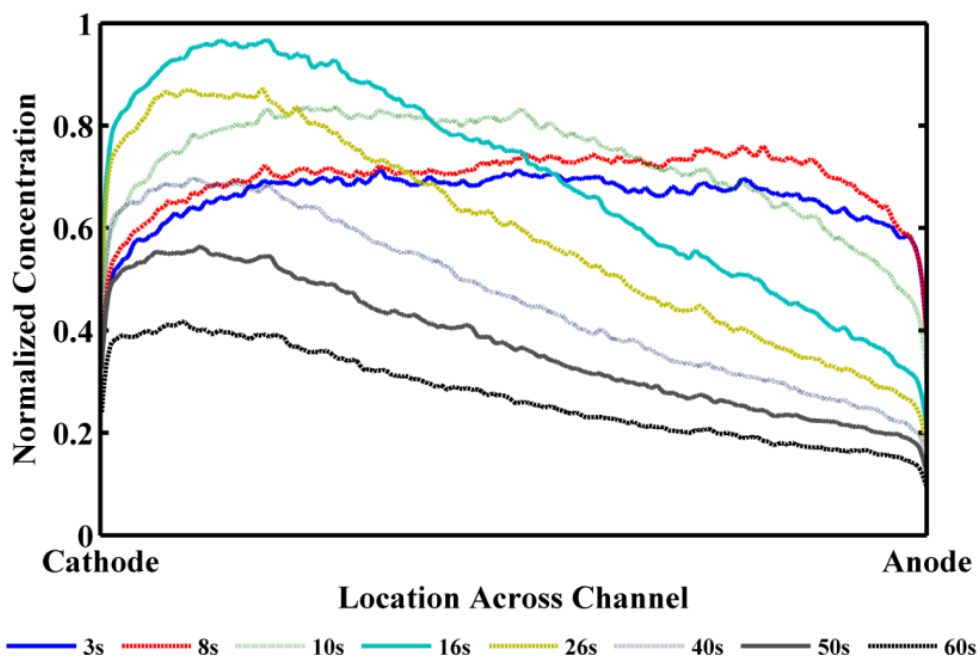


Figure 3.11b: Time dependent concentration profiles within the bulk solution for SRB. The concentration distribution within porous structure is omitted

For a better understanding of the processes occurring during desalination, the temporal variation of the concentration profile across the channel has been provided in Figure 3.11b. As seen in this figure, the concentration across the channel is symmetric at the beginning of desalination ($t = 3\text{s}$), and the concentration gradients on both sides of the channel indicate that SRB ions are diffusing into the anode and cathode. As the electric field is applied, it is seen that the bulk concentration increases, more significantly on the anode side ($t = 8\text{s}$). This is due to the fact that application of the electric field repels the SRB ions from within the porous anode. Membrane CDI (MCDI) processes have been specifically developed to overcome this coion expulsion effect and to increase adsorption efficiency (Biesheuvel, Zhao, Porada, & van der Wal, 2011; Y.-J. Kim & Choi, 2010). After this initial increase, it is seen that the SRB concentration peak shifts towards the cathode, indicating electro migration of ions within the bulk solution ($t = 10\text{s}, 16\text{s}$). This is followed by the electromigration of ions from the bulk solution to the pores of the anode, which results in decrease of overall bulk concentration ($t = 26\text{s}$). It is observed that after this initial transient period, the shape of bulk concentration profile does not change significantly, but the values decrease with time due to electrosorption inside the porous electrodes, until the whole electrode is saturated by adsorbed ions and the electric field is completely shielded by the electrical double layer (EDL).

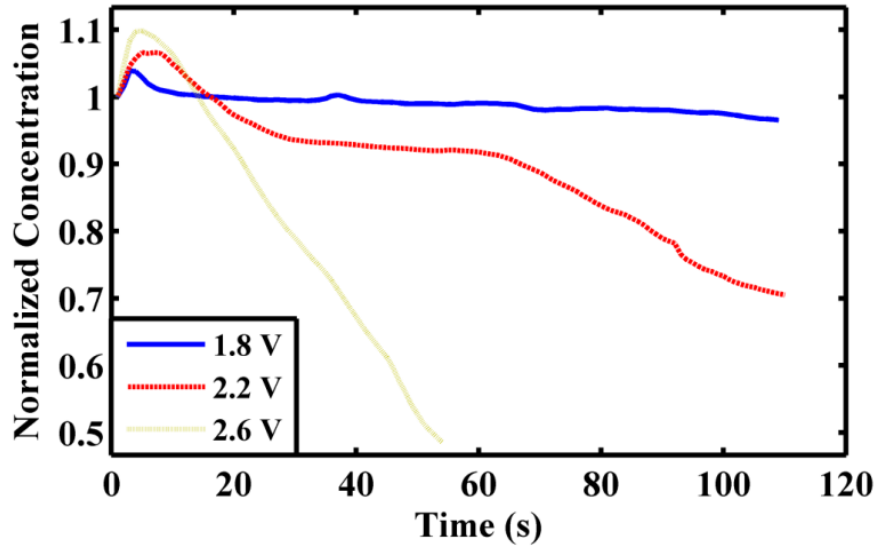


Figure 3.12a: Bulk SRB concentration for desalination tests at different CDI cell potentials. Coion expulsion seen in the first 15 s and rate of concentration decrease is directly related to CDI cell potential

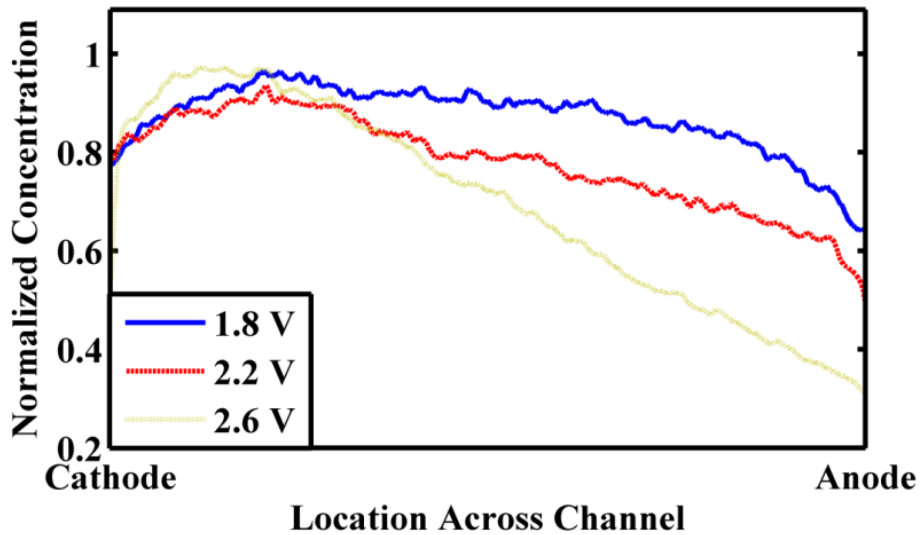


Figure 3.12b: Concentration profiles during desalination tests performed at different CDI cell potentials. It is seen that the shift of concentration peak and the asymmetry in concentration profile is directly related to CDI cell potential

After seeing that CDI cell potential affected the bulk concentration distribution significantly, tests were run at various CDI cell potentials to characterize this effect. In Figure 3.12a, time dependent average bulk concentrations are shown for desalination tests performed at 1.8, 2.2 and 2.6 V. The coion expulsion effect is seen as an initial increase of bulk solution concentrations in the first 10 s for all three tests. In addition, it is seen that the coion expulsion and counterion adsorption rates are almost the same between 30s and 60s for desalination test with 2.2 V applied voltage, resulting in an almost constant bulk solution concentration during this period. After 60s, the coions in the anode are almost depleted and the concentration decrease is driven by counterion adsorption into the cathode. The important difference between these three tests is the rate of concentration decrease, or the rate of ionic adsorption, after this initial period, which is found as 0.008 $\mu\text{M/s}$, 0.088 $\mu\text{M/s}$ and 0.212 $\mu\text{M/s}$ for 1.8, 2.2 and 2.6 V respectively. An “adsorption velocity” term to model this initial adsorption rate has been used previously by (Rios Perez et al., 2013) and it was assumed that this adsorption rate would decrease linearly with increasing electrode concentration, due to saturation and EDL shielding effects. In this study, it is shown that the electrosorption rate is also strongly dependent on the CDI cell potential. To observe the effect of CDI cell potential, and thus the adsorption rate, on bulk solution concentration, normalized concentration profiles obtained after the initial coion expulsion period are also illustrated in Figure 3.12b for desalination at 1.8, 2.2 and 2.6 V CDI cell potentials. The concentration profiles provided in Figure 3.12b indicate that the asymmetry and the shift of peak in bulk solution concentration are directly related to CDI cell potential and thus the electrosorption rate. These results are intuitive, since the concentration accumulation at the cathode / bulk solution interface is expected to be more pronounced at high ionic flux conditions.

A sample desalination / regeneration test at 2.6 V CDI cell potential is provided in supplemental video 1. Initial coion expulsion, shift of concentration peak towards the cathode and decrease of the overall bulk solution concentration can all be seen in this video. To assure that bulk solution concentration decrease was not due to photobleaching, deterioration of fluorophores after extended excitation, desalination was stopped after 65 s (around 13 s in supplemental video 1). It was seen that as soon as desalination stopped, the bulk solution concentration increased back to approximately the same level before desalination. Therefore, it was verified that the bulk concentration decrease is indeed due to electro migration of SRB ions into the porous electrode.

3.2.2 Single Fluorophore LIF: Migration of Ions within Porous Electrodes

Second type of single fluorophore LIF experiments were performed to observe the migration of ions within porous electrodes and the average bulk concentration decrease due to electrosorption. Two sample 2D concentration distributions obtained before and during desalination experiments are illustrated in Figures 3.13a and 3.13b for SRB. In Figure 3.13a, it is seen that SRB has diffused into the porous electrodes at the beginning of desalination experiments, but the bulk concentration is still higher than electrode concentration. The electrode and bulk concentration should equalize provided that enough time is provided for diffusion, but the large width of the porous structure and low bulk solution concentration means very large diffusive time constants. Therefore, experiments are started after 10 minutes of stabilization. In Figure 3.13b, it is seen that concentration within the porous electrodes have increased and the average bulk solution concentration has decreased due to adsorption of ions within the porous electrodes. In addition, the ions within the porous structure have a nonuniform distribution, with higher

concentration deeper into the electrode and lower concentration close to the electrode / bulk solution interface.

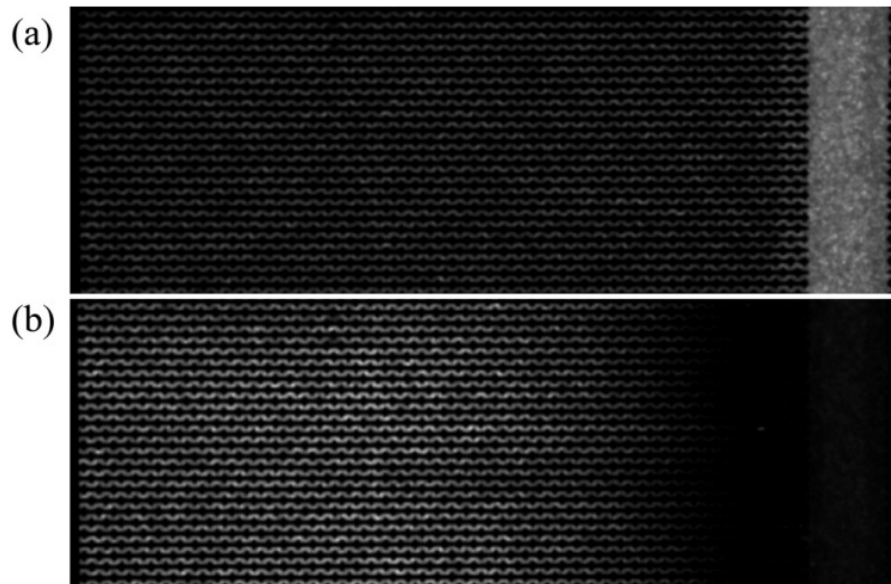


Figure 3.13: 2D concentration profiles for SRB before (a) and during (b) desalination. Concentration within the electrode rises with ionic adsorption, whereas bulk concentration decreases. The lowest concentration is seen in the depletion region

The transient behavior of SRB concentration profile within the bulk solution and within the porous electrode during desalination is provided in Figure 3.14a, together with the NRMSD associated with each concentration profile. It is seen that the concentration profiles at different instants during desalination process can be captured with less than 10.4% NRMSD, using the data processing method detailed in section 2.4. As the electric potential is applied, ions inside the porous electrode start migrating deeper into the porous electrode, leaving a region of low concentration behind them, close to the electrode / bulk solution interface. This depletion region drives the ions from the bulk solution into the electrode by concentration diffusion. In time, the ions adsorbed from the bulk solution cause an increase in average electrode concentration and cause the

depletion layer to get smaller ($t=60\text{s}-240\text{s}$). In Figure 13a ($t=240\text{s}$), it is seen that the depletion region still exists, while the bulk concentration is almost zero, meaning that the electrode is not saturated and has the capacity to adsorb more ions. When the electrode is fully saturated, it is expected that concentration in the depletion region is almost the same as bulk concentration, so the ion flux from the bulk solution towards the electrode is zero. Such a depletion effect at the electrode / bulk solution interface has been postulated in the work of (Bazant et al., 2004) and has been used by (Rios Perez et al., 2013) to model the adsorption flux. The existence of a depletion region is verified by the actual concentration profiles obtained in this study, but it was seen that it actually occurred inside the porous electrode. Imaging of the porous electrode close to the electrode / bulk solution interface is also performed by a 10x objective and presented in supplemental video 2 to show the formation of depletion region in more detail.

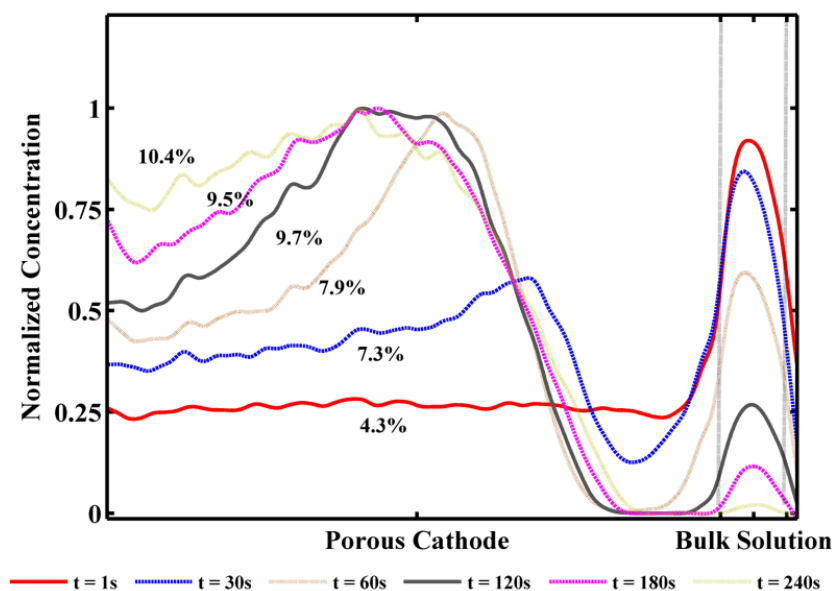


Figure 3.14a: Time dependent concentration distribution within the porous electrode and the bulk solution. Formation of depletion region ($t=30\text{s}-60\text{s}$), decrease in bulk solution concentration and increase in electrode concentration can be seen. NRMSD values are provided with each concentration profile

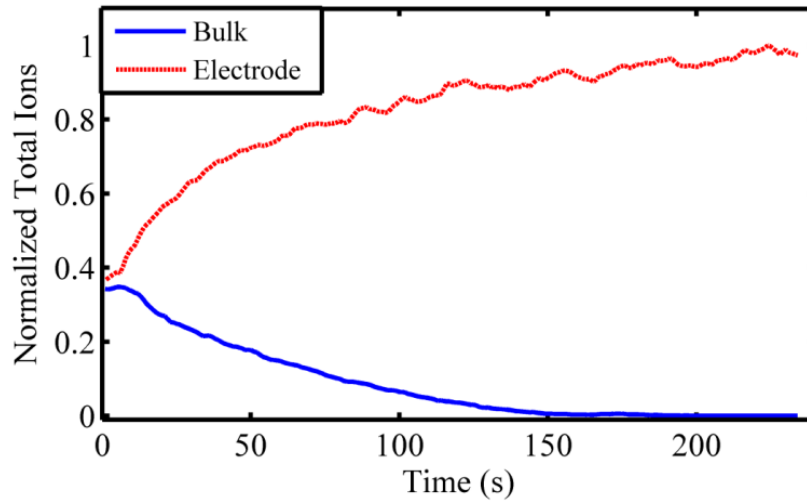


Figure 3.14b: Total amount of ions stored in the bulk solution and within the porous electrode a function of time during desalination

In addition to investigating the concentration profiles, the total amount of ions within the solution and the porous electrode were also calculated and presented in Figure 3.14b. It is also seen from this figure that the amount of ions in the bulk solution does not decrease in the first 10 s despite the adsorption inside the porous electrode, illustrating the effect of coion expulsion from the anode. After this initial period, the number of ions in the bulk solution decays while the amount of ions in the porous electrode increases. After 200 s, it is seen that the amount of ions within the bulk solution is approximately zero and the amount of ions within the porous electrode is almost steady at its maximum. It should be noted that the increase in the amount of ions within the cathode is more than the decrease of ions within the bulk solution. This is due to the fact that there are SRB ions within the anode at the beginning of desalination and these ions are also adsorbed within the pores of the cathode. If the ions are distributed evenly between anode and cathode at the beginning of desalination, the amount of ions within the cathode at the end of desalination is expected to be twice the initial amount in the cathode plus the initial

amount of ions within the bulk solution. It is seen that the measured change in the amount of ions is 8.2% less than this expected change, which indicates that the initial distribution of ions were not perfectly homogeneous. This might be the case due to imperfect regeneration of porous electrodes and remnant ions from a previous test.

3.2.3 Dual Fluorophore LIF

Dual fluorophore LIF experiments were performed to observe simultaneous ionic migration of two oppositely charged species within the bulk solution and within the porous electrodes. A sample concentration profile observed 150 s after the application of electric field is provided in Figure 3.15a and the asymmetric concentration profile observed in previous LIF experiments can also be seen in Figure 3.15b, which depicts the concentration along a straight line drawn through the middle of a single pore. The distribution of concentrations within porous electrodes indicates that coions that are present within the electrodes before desalination process are repelled by the application of the electric field and counterions are adsorbed within the porous electrodes. It is seen that the bulk concentration change of Fluorescein is significantly more than that of SRB. This is expected to be due to the effects of molecular size and mobility, which favor the electro migration of Fluorescein ($C_{20}H_{12}O_5$) over SRB ($C_{27}H_{30}N_2O_7S_2$). This expectation is supported by the findings of (Werner, Konarev, Svergun, & Hahn, 2009) and (Milanova et al., 2011), which indicate an order of magnitude difference between the diffusion coefficients of Fluorescein ($9.3 \cdot 10^{-10} \text{ m}^2/\text{s}$) and SRB ($0.7 \cdot 10^{-10} \text{ m}^2/\text{s}$). It is also thought that the counterions released by Fluorescein upon dissolving in water impede SRB adsorption more, because of the higher Fluorescein concentration. This is observed as a weak depletion region, and thus smaller adsorption flux, for SRB and a strong one for Fluorescein.

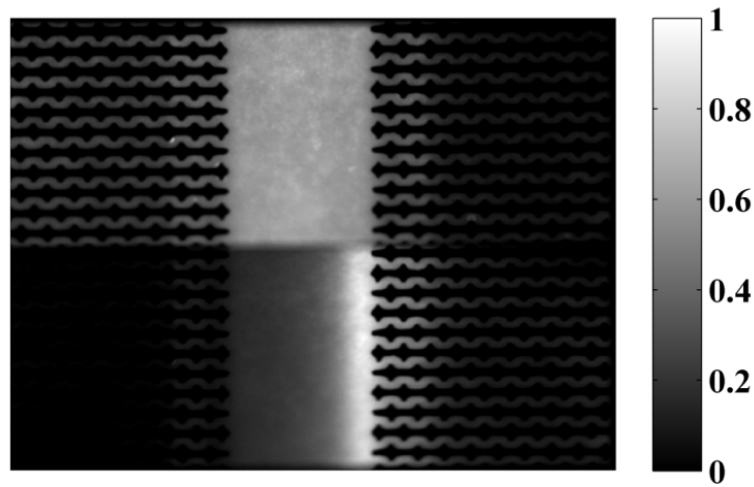


Figure 3.15a: Snapshot of the model CDI cell 150 s after beginning of desalination. SRB (top) and Fluorescein (bottom) concentrations

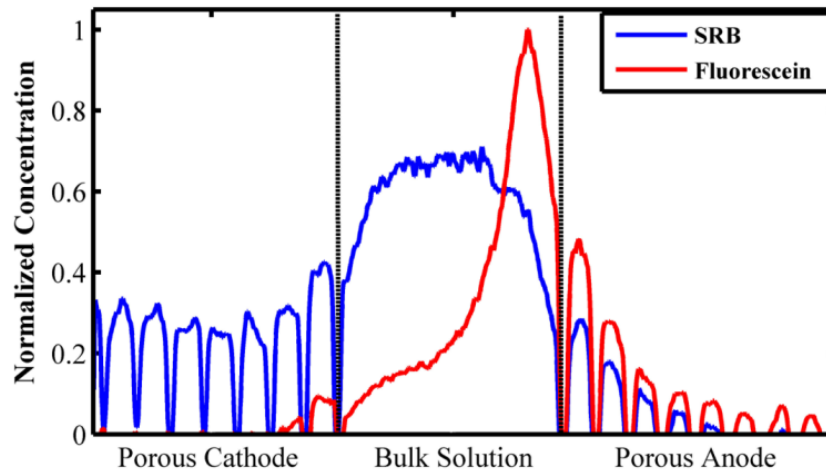


Figure 3.15b: Concentration profile across the channel section in Figure 14a. SRB is depleted in anode and concentrated within cathode, with almost uniform bulk concentration. Fluorescein is depleted in the cathode and concentrated within the anode, with most of the Fluorescein concentrated at anode / bulk solution interface

A time lapse of the first 150 s of desalination cycle is provided in Figure 3.16. It is seen that both dyes have diffused into both electrodes by diffusion at the beginning of desalination ($t=3s$). As the electric potential is applied, both SRB and Fluorescein are

expelled from anode and cathode respectively. However, the electro migration of Fluorescein from the bulk solution into the anode is significantly faster than electromigration of SRB in the opposite direction ($t=44s$). At 100 s, it is seen that the highly concentrated Fluorescein ions within anode have started to migrate deeper into the porous electrode, creating a stronger depletion region, whereas the depletion region in Sulforhodamine is much weaker. This effect is also observed in bulk solution concentration distributions. It is seen that Fluorescein ions within the bulk start to build up at the anode / bulk solution interface, whereas SRB ions are more uniformly distributed among bulk solution. After 150 s of desalination, it is seen that Fluorescein ions have been significantly concentrated at the anode/ bulk solution interface with a strong depletion layer inside the electrode, indicating high adsorption flux into the electrode. After this point, the shape of either concentration profile does not change noticeably, but the average concentrations decrease due to electro migration into porous electrodes. This behavior observed during desalination experiments underscore the selectivity of CDI towards higher mobility ions.

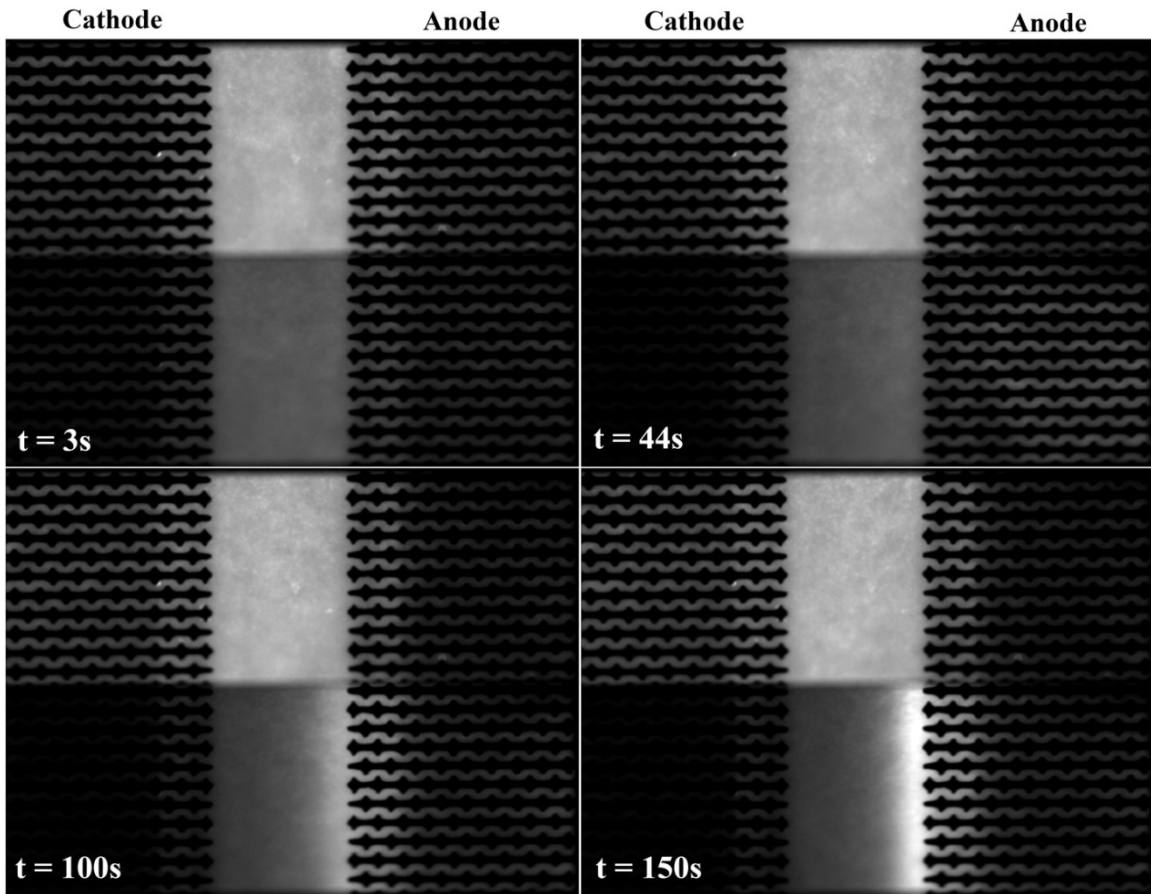


Figure 3.16: Time lapse of desalination (0s - 150s). (t = 3s) Almost uniform concentration distribution at the beginning of desalination. (t=44s) Coions are expelled from both electrodes and Fluorescein concentration in anode increases significantly. (t=100s) Fluorescein ions migrate further into the electrode to form a depletion region (t=150s) Bulk SRB concentration has not changed noticeably, whereas bulk Fluorescein concentration has shifted towards the anode

Chapter 4: Conclusion

The research performed for this thesis includes two novel approaches to capacitive deionization. The first approach is focused on the application of CDI process to various conditions, whereas the second approach is focused on understanding the fundamentals of CDI process through optical measurements. These different approaches are presented in two chapters.

In the first part of this research, a novel methodology to determine the most favorable operational conditions for a capacitive deionization cell functioning at alternating transient desalination-regeneration processes is presented. Also, three evaluation criteria based on the energetic performance of the system were proposed. These metrics were then used to evaluate the effects of CDI system size and inlet solution concentration on the overall system performance. The results presented in this study suggest that switching the CDI system from desalination to regeneration and *vice versa* to maximize the amount of ions adsorbed per unit energy (t_3) maximizes the thermodynamic efficiency of the system. On the other hand, timing the system to maximize the average adsorption rate during desalination (t_2) usually results in highest number of ions adsorbed per input energy per volume of solution treated. These two findings indicate that there exists two optimal operational points for a CDI system: maximum efficiency and maximum adsorption rate. One can choose to operate the system at either of these two points or somewhere in between, depending on the critical requirements, and the results indicate a trade-off between thermodynamic efficiency and adsorption rate. It was also seen that timing the system according to maxima and minima of outlet concentration might be the simplest solution, but it results in the lowest system performance according to all the metrics, except energy recovery ratio, which was shown to be insufficient by

itself to measure the energetic performance. Experimental results indicate that energy recovery ratio is directly proportional to inlet solution concentration, due to the effect of incomplete regeneration and remnant ions from previous cycles. On the other hand, thermodynamic efficiency is inversely proportional to inlet solution concentration, which points to deteriorating system performance at higher salinity levels. Therefore, it can be said that there exist a higher limit of solution concentration which can be economically and practically processed by a CDI system of certain size. The results also indicate that increasing system size provides an increase in thermodynamic efficiency. This was seen to be due to the higher system capacity enabling a more significant drop in outlet conductivity during desalination. This is a promising result which should provide motivation to build larger scale CDI systems and to make commercial CDI systems a reality.

In the second part of this research, a novel microfluidic device was fabricated to be used in study of ionic transport in capacitive deionization process. The fabricated device features flow channels, pseudo-porous electrodes and electrical contacts integrated on a silicon-on-insulator chip. The simultaneous transport of anions and cations within this device is visualized by laser induced fluorescence, using cationic SRB and anionic Fluorescein dyes. The fluorescence emission from these dyes were spectrally separated and used for tracing the two oppositely charged particles independently. Single and dual fluorophore desalination tests were run to prove that the concept works. Effects of electrical field on bulk solution concentration profile and electro migration of ions within porous electrodes were studied by single fluorophore LIF experiments. Transient concentration profiles were obtained within the porous electrodes and the effect of CDI cell potential on electrosorption rate is quantified. Simultaneous concentration measurements for both anions and cations were also performed by dual fluorophore LIF

tests and the effects of ion mobility on transport were illustrated. It was seen that fluorophores with similar size and mobility should be chosen in order to observe comparable electrosorption of both anions and cations. This study serves to be the first in providing visual access into the CDI process. Future work should be focused on fabrication of higher capacity porous electrodes to represent the actual porous electrode structures more accurately and possibly to come up with a CDI-on-a-chip application.

References

- Al-Shammiri, M., & Safar, M. (1999). Multi-effect distillation plants: state of the art. [doi: 10.1016/S0011-9164(99)00154-X]. *Desalination*, 126(1,Äi3), 45-59.
- Albaugh, K. B., Cade, P. E., & Rasmussen, D. H. (1988, 6-9 Jun 1988). *Mechanisms of anodic bonding of silicon to pyrex glass*. Paper presented at the Solid-State Sensor and Actuator Workshop, 1988. Technical Digest., IEEE.
- Anderson, M. A., Cudero, A. L., & Palma, J. (2010). Capacitive deionization as an electrochemical means of saving energy and delivering clean water. Comparison to present desalination practices: Will it compete? [doi: 10.1016/j.electacta.2010.02.012]. *Electrochimica Acta*, 55(12), 3845-3856.
- Atkins, P., & de Paula, J. (2006). *Atkin's Physical Chemistry* (Eighth ed.): Freeman, W. H. & Company.
- Bazant, M. Z., Thornton, K., & Ajdari, A. (2004). Diffuse-charge dynamics in electrochemical systems. *Physical Review E*, 70(2), 021506.
- Bejan, A. (2006). *Advanced Engineering Thermodynamics* (3rd ed.): Wiley, John & Sons, Inc.
- Biesheuvel, P. M., Fu, Y., & Bazant, M. Z. (2011). Diffuse charge and Faradaic reactions in porous electrodes. *Physical Review E*, 83(6), 061507.
- Biesheuvel, P. M., van Limpt, B., & van der Wal, A. (2009). Dynamic Adsorption/Desorption Process Model for Capacitive Deionization. [doi: 10.1021/jp809644s]. *The Journal of Physical Chemistry C*, 113(14), 5636-5640. doi: 10.1021/jp809644s
- Biesheuvel, P. M., Zhao, R., Porada, S., & van der Wal, A. (2011). Theory of membrane capacitive deionization including the effect of the electrode pore space. *Journal of Colloid and Interface Science*, 360(1), 239-248.
- Bouhadana, Y., Avraham, E., Noked, M., Ben-Tzion, M., Soffer, A., & Aurbach, D. (2011). Capacitive Deionization of NaCl Solutions at Non-Steady-State Conditions: Inversion Functionality of the Carbon Electrodes. *The Journal of Physical Chemistry C*, 115(33), 16567-16573. doi: 10.1021/jp2047486

- Bouhadana, Y., Ben-Tzion, M., Soffer, A., & Aurbach, D. (2011). A control system for operating and investigating reactors: The demonstration of parasitic reactions in the water desalination by capacitive de-ionization. *Desalination*, 268(1–3), 253-261. doi: <http://dx.doi.org/10.1016/j.desal.2010.10.037>
- Bureau, U. S. C. (2012, May 31, 2012). U.S. & World Population Clocks Retrieved May 15, 2012, 2012, from <http://www.census.gov/main/www/popclock.html>
- Carroll, B., & Hidrovo, C. (2012). Experimental Investigation of Inertial Mixing in Colliding Droplets. *Heat Transfer Engineering*, 34(2-3), 120-130. doi: 10.1080/01457632.2013.703087
- Clifton, R. L., Rios Perez, C. A., Naylor, R., & Hidrovo, C. (2012, July 8-12, 2012). *Characterization of ion transport and -sorption in a carbon based porous electrode for desalination purposes*. Paper presented at the 10th International Conference on Nanochannels, Microchannels, and Minichannels, Rio Grande, Puerto Rico.
- Coping with Water Scarcity: Challenge of the 21st Century. (2007). Retrieved from Food and Agriculture Organization of the United Nations website: <http://www.fao.org/nr/water/docs/escarcity.pdf>
- Demirer, O. N., Clifton, R. L., Perez, C. A. R., Naylor, R., & Hidrovo, C. (2013). Characterization of Ion Transport and-Sorption in a Carbon Based Porous Electrode for Desalination Purposes. *ASME J. Fluids Eng.*(accepted for publication)(Article DOI Number: 10.1115/1.4023294).
- Demirer, O. N., & Hidrovo, C. H. (2013). Laser-induced fluorescence visualization of ion transport in a pseudo-porous capacitive deionization microstructure. *Microfluidics and Nanofluidics*, 1-14.
- Demirer, O. N., Naylor, R. M., Rios Perez, C. A., Wilkes, E., & Hidrovo, C. (2013). Energetic performance optimization of a capacitive deionization system operating with transient cycles and brackish water. *Desalination*, 314(0), 130-138. doi: <http://dx.doi.org/10.1016/j.desal.2013.01.014>

- Dermentzis, K., & Ouzounis, K. (2008). Continuous capacitive deionization-electrodialysis reversal through electrostatic shielding for desalination and deionization of water. [doi: DOI: 10.1016/j.electacta.2008.05.026]. *Electrochimica Acta*, 53(24), 7123-7130.
- Greenlee, L. F., Lawler, D. F., Freeman, B. D., Marrot, B., & Moulin, P. (2009). Reverse osmosis desalination: Water sources, technology, and today's challenges. *Water Research*, 43(9), 2317-2348. doi: 10.1016/j.watres.2009.03.010
- Jayaraj, B., Desai, V., Lee, C., & Sohn, Y. (2004). Electrochemical impedance spectroscopy of porous ZrO_2 -8wt.% Y_2O_3 and thermally grown oxide on nickel aluminide. *Materials Science and Engineering: A*, 372(1), 278-286.
- Johnson, A. M., & Newman, J. (1971). Desalting by Means of Porous Carbon Electrodes. *Journal of The Electrochemical Society*, 118(3), 510-517.
- Kim, M., & Yoda, M. (2010). Dual-tracer fluorescence thermometry measurements in a heated channel. *Experiments in Fluids*, 49(1), 257-266. doi: 10.1007/s00348-010-0853-9
- Kim, Y.-J., & Choi, J.-H. (2010). Enhanced desalination efficiency in capacitive deionization with an ion-selective membrane. *Separation and Purification Technology*, 71(1), 70-75. doi: 10.1016/j.seppur.2009.10.026
- Lee, T. M. H., Lee, D. H. Y., Liaw, C. Y. N., Lao, A. I. K., & Hsing, I. M. (2000). Detailed characterization of anodic bonding process between glass and thin-film coated silicon substrates. *Sensors and Actuators A: Physical*, 86(1-2), 103-107. doi: 10.1016/S0924-4247(00)00418-0
- Lim, J.-A., Park, N.-S., Park, J.-S., & Choi, J.-H. (2009a). Fabrication and characterization of a porous carbon electrode for desalination of brackish water. *Desalination*, 238(1-3), 37-42.
- Lim, J.-A., Park, N.-S., Park, J.-S., & Choi, J.-H. (2009b). Fabrication and characterization of a porous carbon electrode for desalination of brackish water. [doi: DOI: 10.1016/j.desal.2008.01.033]. *Desalination*, 238(1-3), 37-42.

- Malaeb, L., & Ayoub, G. M. (2011). Reverse osmosis technology for water treatment: State of the art review. *Desalination*, 267(1), 1-8. doi: 10.1016/j.desal.2010.09.001
- McGlade, J., Werner, B., Young, M., Matlock, M., Jefferies, D., Sonnemann, G., Aldaya, M., Pfister, S., Berger, M., Farrell, C., Hyde, K., Wackernagel, M., Hoekstra, A., Mathews, R., Liu, J., Ercin, E., Weber, J.L., Alfieri, A., Martinez-Lagunes, R., & Edens, B., Schulte, P., von Wirén-Lehr, S., Gee, D. (2012). Measuring water use in a green economy: UNEP.
- Milanova, D., Chambers, R. D., Bahga, S. S., & Santiago, J. G. (2011). Electrophoretic mobility measurements of fluorescent dyes using on-chip capillary electrophoresis. *ELECTROPHORESIS*, 32(22), 3286-3294. doi: 10.1002/elps.201100210
- Mossad, M., & Zou, L. (2012). A study of the capacitive deionisation performance under various operational conditions. *Journal of Hazardous Materials*, 213–214(0), 491-497. doi: 10.1016/j.jhazmat.2012.02.036
- Newman, J. (1968). ENGINEERING DESIGN OF ELECTROCHEMICAL SYSTEMS. *Industrial & Engineering Chemistry*, 60(4), 12-27. doi: 10.1021/ie50700a005
- Park, K.-K., Lee, J.-B., Park, P.-Y., Yoon, S.-W., Moon, J.-S., Eum, H.-M., & Lee, C.-W. (2007). Development of a carbon sheet electrode for electrosorption desalination. [doi: DOI: 10.1016/j.desal.2006.04.051]. *Desalination*, 206(1-3), 86-91.
- Pekala, R. W., Farmer, J. C., Alviso, C. T., Tran, T. D., Mayer, S. T., Miller, J. M., & Dunn, B. (1998). Carbon aerogels for electrochemical applications. *Journal of Non-Crystalline Solids*, 225(0), 74-80. doi: 10.1016/s0022-3093(98)00011-8
- Piacentino, A., & Cardona, E. (2010). Advanced energetics of a Multiple-Effects-Evaporation (MEE) desalination plant. Part II: Potential of the cost formation process and prospects for energy saving by process integration. *Desalination*, 259(1–3), 44-52. doi: <http://dx.doi.org/10.1016/j.desal.2010.04.037>
- Prakash, S., Yeom, J., Jin, N., Adesida, I., & Shannon, M. A. (2006). Characterization of ionic transport at the nanoscale. *Proceedings of the Institution of Mechanical*

- Engineers, Part N: Journal of Nanoengineering and Nanosystems*, 220(2), 45-52.
doi: 10.1243/17403499jnn91
- Quaglio, M., Canavese, G., Giuri, E., Marasso, S., Perrone, D., Cocuzza, M., & Pirri, C. (2008). Evaluation of different PDMS interconnection solutions for silicon, Pyrex and COC microfluidic chips. *Journal of Micromechanics and Microengineering*, 18(5), 055012.
- Ray, K., & Nakahara, H. (2001). Adsorption of Sulforhodamine Dyes in Cationic Langmuir–Blodgett Films: Spectroscopic and Structural Studies. *The Journal of Physical Chemistry B*, 106(1), 92-100. doi: 10.1021/jp011946d
- Rios Perez, C. A., Demirer, O. N., Clifton, R. L., Naylor, R., & Hidrovo, C. (2013). Macro analysis of the electro adsorption process in low concentration NaCl solutions for water desalination applications. *Journal of The Electrochemical Society*, 160(3), E13-E21.
- Ryu, J.-H., Kim, T.-J., Lee, T.-Y., & Lee, I.-B. (2010). A study on modeling and simulation of capacitive deionization process for wastewater treatment. *Journal of the Taiwan Institute of Chemical Engineers*, 41(4), 506-511. doi: 10.1016/j.jtice.2010.04.003
- Shiklomanov, I. A. (1999). World Water Resources: Modern Assessment and Outlook for the 21st Century (S. H. Institute, Trans.): UNESCO - Federal Service of Russia for Hydrometeorology & Environment Monitoring.
- Song, A., Zhang, J., Zhang, M., Shen, T., & Tang, J. a. (2000). Spectral properties and structure of fluorescein and its alkyl derivatives in micelles. *Colloids and Surfaces A: Physicochemical and Engineering Aspects*, 167(3), 253-262. doi: [http://dx.doi.org/10.1016/S0927-7757\(99\)00313-1](http://dx.doi.org/10.1016/S0927-7757(99)00313-1)
- Spiegler, K. S., & El-Sayed, Y. M. (2001). The energetics of desalination processes. *Desalination*, 134(1-3), 109-128.
- Technology, C. o. A. D., & Council, N. R. (2008). *Desalination: A National Perspective*: The National Academies Press.

- Villar, I., Roldan, S., Ruiz, V., Granda, M., Blanco, C., Menéndez, R., & Santamaría, R. (2010). Capacitive Deionization of NaCl Solutions with Modified Activated Carbon Electrodes†. *Energy & Fuels*, *24*(6), 3329-3333. doi: 10.1021/ef901453q
- Wang, L., Wang, M., Huang, Z.-H., Cui, T., Gui, X., Kang, F., . . . Wu, D. (2011). Capacitive deionization of NaCl solutions using carbon nanotube sponge electrodes. *Journal of Materials Chemistry*, *21*(45), 18295-18299.
- Wang, Z., Dou, B., Zheng, L., Zhang, G., Liu, Z., & Hao, Z. (2012). Effective desalination by capacitive deionization with functional graphene nanocomposite as novel electrode material. *Desalination*, *299*(0), 96-102. doi: <http://dx.doi.org/10.1016/j.desal.2012.05.028>
- Welgemoed, T. J., & Schutte, C. F. (2005). Capacitive Deionization Technology(TM): An alternative desalination solution. [doi: DOI: 10.1016/j.desal.2005.02.054]. *Desalination*, *183*(1-3), 327-340.
- Werner, A., Konarev, P. V., Svergun, D. I., & Hahn, U. (2009). Characterization of a fluorophore binding RNA aptamer by fluorescence correlation spectroscopy and small angle X-ray scattering. *Analytical Biochemistry*, *389*(1), 52-62. doi: <http://dx.doi.org/10.1016/j.ab.2009.03.018>
- Xu, P., Drewes, J. E., Heil, D., & Wang, G. (2008). Treatment of brackish produced water using carbon aerogel-based capacitive deionization technology. *Water Research*, *42*(10–11), 2605-2617. doi: 10.1016/j.watres.2008.01.011
- Yang, J., Zou, L., Song, H., & Hao, Z. (2011). Development of novel MnO₂/nanoporous carbon composite electrodes in capacitive deionization technology. *Desalination*, *276*(1–3), 199-206. doi: <http://dx.doi.org/10.1016/j.desal.2011.03.044>